



Spectral Method Applied to Unstructured Thermochemical Non-Equilibrium Reentry Flows in 2D: Five Species

Edisson Sávio de Góes Maciel

Rua Santa Clara, 245 – Cx. Postal: 2029 – 12.243-970 – São José dos Campos – SP – Brazil

Abstract In the present work, a study involving aspectral method to solve the reactive Euler and Navier-Stokes equations is performed. The Euler and Navier-Stokes equations, in conservative and finite volume contexts, employing unstructured spatial discretization, on a condition of thermochemical non-equilibrium, are studied. The spectral method presented in this work employs collocation points and variants of Chebyshev and Legendre interpolation functions are analyzed. High-order studies are accomplished to verify the accuracy of the spectral method. The “hot gas” hypersonic flows around a blunt body, and around a double ellipse in two-dimensions are simulated. The Van Leer and the Liou and Steffen Jr. flux vector splitting algorithms are applied to execute the numerical experiments. The Euler backward integration method is employed to march the schemes in time. The convergence process is accelerated to steady state condition through a spatially variable time step procedure, which has proved effective gains in terms of computational acceleration (see Maciel). The reactive simulations involve Earth atmosphere chemical model of five species and seventeen reactions, based on the Saxena and Nair model. N, O, N₂, O₂, and NO species are used to accomplish the numerical comparisons. The results have indicated that the Chebyshev collocation point variants are more accurate in terms of stagnation pressure estimations, with errors inferior to 17.00% in the worst case, and in terms of lift coefficient estimations. Moreover, the Legendre collocation point variants are more computationally efficient.

Keywords Spectral method; hypersonic flow; thermochemical non-equilibrium reentry flows; reactive Euler; Navier-Stokes equations; high order accuracy; Van Leer scheme; Liou and Steffen Jr. scheme

1. Introduction

There are several approaches for computationally modeling fluid dynamics. These include finite difference, finite element, and spectral methods to name a few. Finite element and finite difference methods are frequently used and offer a wide range of well-known numerical schemes. These schemes can vary in terms of computational accuracy, but are typically of lower order of accuracy. If a more accurate solution is desired, it is common practice to refine the mesh either globally or in a region of interest. This can often be a complicated or time consuming process as global mesh refinement will greatly increase the computation time while local refinement requires an elaborated refinement operation [1].

Alternatively, polynomial refinement has been used to improve the solution accuracy and has been shown to converge more quickly than mesh refinement in some cases [2-3]. For finite difference methods, polynomial refinement is performed by including neighboring node values in a higher order polynomial [4]. This can increase the complexity of the scheme especially near the boundaries where nodes do not exist to construct the higher order polynomials. Finite element methods instead increase the number of unknown values within the cell itself to construct a higher order solution [5].

A scheme with a very high formal order of accuracy will not necessarily always produce the highest resolution. [6] demonstrated that a spectral-like scheme with a formal fourth-order accuracy produced a much more highly



resolved solution than schemes with higher formal orders of accuracy when comparing modified wave numbers. Therefore, formal order of accuracy does not provide a comprehensive basis for selecting the best solution procedure. State-of-art methods such as spectral methods fall into this category.

Spectral methods are considered a class of solution techniques using sets of known functions to solve differential equations [7]. Such methods are generally considered high order and capable of obtaining solutions with a high resolution. Unlike finite-difference and finite-element methods, spectral methods utilize an expansion in terms of global, rather than local, basis functions to represent the solution of a differential equation. When properly applied, these techniques accurately resolve phenomena on the scale of the mesh spacing. The order of truncation error decay with mesh refinement is also higher than which can be achieved with finite-difference and finite-element methods. For problems with smooth solutions, it is possible to produce spectral method whose truncation error goes to zero as faster than any finite power of the mesh spacing (exponential convergence).

Spectral methods may be viewed as an extreme development of the class of discretization schemes known by the generic name of method of weighted residuals (MWR) [8]. The key elements of the MWR are the trial functions (also called the expansion or approximating functions) and the test functions (also known as weighted functions). The trial functions are used as the basis functions for a truncated series expansion of the solution that, when substituted into the differential equation, produces the residual. The test functions are used to enforce the minimization of the residual.

The choice of the trial functions is what distinguishes the spectral methods from the element and finite difference methods. The trial functions for spectral methods are infinitely differentiable global functions (Typically, they are tensor products of the eigenfunctions of singular Sturm-Liouville problems). In the case of finite element methods, the domain is divided into small elements and a trial function is specified in each element. The trial functions are thus local in character and well suited for handling complex geometries. The finite difference trial functions are likewise local.

The choice of test function distinguishes between Galerkin and collocation approaches. In the Galerkin approach, the test functions are the same as the trial functions, whereas in the collocation approach the test functions are translated Dirac delta functions. In other words, the Galerkin approach is equivalent to a least-square approximation, whereas the collocation approach requires the differential equations to be solved exactly at the collocation points.

The collocation approach is the simplest of the MWR and appears to have been first used by [9] in his study of electronic energy bands in metals. A few years later, [10] applied this method to the problem of torsion in square prism. [11] developed it as a general method for solving ordinary differential equations. They used a variety of trials functions and an arbitrary distribution of collocation points. The work of [12] established for the first time that a proper choice of the trial functions and the distribution of collocation points are crucial to the accuracy of the solution. Perhaps he should be credited with laying down the foundation of the orthogonal collocation method.

Spectral methods have been used on one-dimensional, compressible flow problems with piecewise linear solutions by [13-14]. These reports demonstrated that spectral methods, when combined with appropriate filtering techniques, can capture one-dimensional shock waves in otherwise featureless flows. A different sort of demonstration was provided by [15]. They exhibited spectral solutions of compressible flows with nontrivial structures in the smooth regions.

Renewed interest in the area of hypersonic flight has brought Computational Fluid Dynamics (CFD) to the forefront of fluid flow research [16]. Many years have seen a quantum leap in advancements made in the areas of computer systems and software which utilize them for problem solving. Sophisticated and accurate numerical algorithms are devised routinely that are capable of handling complex computational problems. Experimental test facilities capable of addressing complicated high-speed flow problems are still scarce because they are too expensive to build and sophisticated measurements techniques appropriate for such problems, such as the non-intrusive laser, are still in the development stage. As a result, CFD has become a vital tool in the flow problem solution.



In high speed flows, any adjustment of chemical composition or thermodynamic equilibrium to a change in local environment requires certain time. This is because the redistribution of chemical species and internal energies require certain number of molecular collisions, and hence a certain characteristic time. Chemical non-equilibrium occurs when the characteristic time for the chemical reactions to reach local equilibrium is of the same order as the characteristic time of the fluid flow. Similarly, thermal non-equilibrium occurs when the characteristic time for translation and various internal energy modes to reach local equilibrium is of the same order as the characteristic time of the fluid flow. Since chemical and thermal changes are the results of collisions between the constituent particles, non-equilibrium effects prevail in high-speed flows in low-density air.

In chemical non-equilibrium flows the mass conservation equation is applied to each of the constituent species in the gas mixture. Therefore, the overall mass conservation equation is replaced by as many species conservation equations as the number of chemical species considered. The assumption of thermal non-equilibrium introduces additional energy conservation equations – one for every additional energy mode. Thus, the number of governing equations for non-equilibrium flow is much bigger compared to those for perfect gas flow. A complete set of governing equations for non-equilibrium flow may be found in [17-18].

The problems of chemical non-equilibrium in the shock layers over vehicles flying at high speeds and high altitudes in the Earth's atmosphere have been discussed by several investigators [19-22]. Most of the existing computer codes for calculating the non-equilibrium reacting flow use the one-temperature model, which assumes that all of the internal energy modes of the gaseous species are in equilibrium with the translational mode [21-22]. It has been pointed out that such a one-temperature description of the flow leads to a substantial overestimation of the rate of equilibrium because of the elevated vibrational temperature [20]. A three-temperature chemical-kinetic model has been proposed by [23] to describe the relaxation phenomena correctly in such a flight regime. However, the model is quite complex and requires many chemical rate parameters which are not yet known. As a compromise between the three-temperature and the conventional one-temperature model, a two-temperature chemical-kinetic model has been developed [24-25], which is designated herein as the TTV model. The TTV model uses one temperature T to characterize both the translational energy of the atoms and molecules and the rotational energy of the molecules, and another temperature T_v to characterize the vibrational energy of the molecules, translational energy of the electrons, and electronic excitation energy of atoms and molecules. The model has been applied to compute the thermodynamic properties behind a normal shock wave in a flow through a constant-area duct [24-25]. Radiation emission from the non-equilibrium flow has been calculated using the Non-equilibrium Air Radiation (NEQAIR) program [26-27]. The flow and the radiation computations have been packaged into a single computer program, the Shock-Tube Radiation Program (STRAP) [25].

Algorithms for solving the Euler equations using a perfect gas model on structured grids in two- and three-dimensions have become widespread in recent years [28-29]. However, these algorithms have shown difficulties in predicting satisfactory results around complex geometries due to mesh irregularities. As a result, attention has turned to the development of solution algorithms on arbitrary unstructured grids. Impressive results have been obtained for a wide range of problems [30-31].

One problem associated with unstructured meshes is the increased difficulty in obtaining smooth higher order spatial approximations to state data at cell interfaces. Two methods have been used to obtain higher order accuracy on unstructured meshes. A method used by several researchers for cell vertex schemes [32-33] was applied to obtain higher order accuracy in a procedure analogous to MUSCL (Monotone Upstream-centered Schemes for Conservation Laws) differencing on a structured mesh. A conventional structured mesh limiter can be employed in this scheme to obtain approximately monotone results near flow discontinuities. The second method, which was proposed by [31], linearly reconstructs the cell averaged data and imposes a monotone preserving limiter to achieve smooth results near flow discontinuities.

In the present work, a study involving a spectral method to solve the reactive Euler and Navier-Stokes equations is performed. The Euler and Navier-Stokes equations, in conservative and finite volume contexts, employing unstructured spatial discretization, on a condition of thermochemical non-equilibrium, are studied. The spectral method presented in this work employs collocation points and variants of Chebyshev and Legendre interpolation functions are analyzed. High-order studies are accomplished to verify the accuracy of the spectral method. The



“hot gas” hypersonic flows around a blunt body, and around a double ellipse in two-dimensions are simulated. The [34-35] flux vector splitting algorithms are applied to execute the numerical experiments. The Euler backward integration method is employed to march the schemes in time. The convergence process is accelerated to steady state condition through a spatially variable time step procedure, which has proved effective gains in terms of computational acceleration [36-37]. The reactive simulations involve Earth atmosphere chemical model of five species and seventeen reactions, based on the [38] model. N, O, N₂, O₂, and NO species are used to accomplish the numerical comparisons. The results have indicated that the Chebyshev collocation point variants are more accurate in terms of stagnation pressure estimations, with errors inferior to 17.00% in the worst case, and in terms of lift coefficient estimations. Moreover, the Legendre collocation point variants are more computationally efficient.

2. Spectral Method

Two classes of techniques for spectral discretization are referred to as tau and collocation methods [39]. The latter technique is used here. In this scheme, the approximation series is determined by satisfying the differential equation exactly at a set of distinct collocation points. The locations of these points in the domain are linked to the choice of basis function. In this study, arbitrary collocation points are implemented. The collocation method is used here since enforcement of boundary conditions and evaluations of nonlinear terms are straightforward. Additionally, some accuracy advantage is seen in the collocation method over the tau method for a number of problems [39]. The series expansion for a function $Q(x)$ may be represented as

$$Q_N(x) = \sum_{n=0}^N \hat{Q}_n B_n(x), \quad (1)$$

where $B_n(x)$ are the basis functions and N is the total number of nodes employed in the interpolation process (It is also the order of accuracy of the spectral method). The coefficients \hat{Q}_n are often termed the spectrum of $Q_N(x)$. One common technique used to evaluate the spectrum is to consider Eq. (1) as an interpolation series representing $Q(x)$. The interpolation “nodes” of such series are the collocation points of the method. For a scheme based on Chebyshev collocation, the basis functions are:

$$B_n(x) = T_n(x) = 2xP_{n-1}(x) - P_{n-2}(x), \quad n \geq 2, \quad (2)$$

with: $P_0(x) = 1$ and $P_1(x) = x$. The Chebyshev-Gauss-Lobatto standard collocation points are

$$x_l = \cos\left(\frac{\pi l}{N}\right), \quad l = 0, 1, \dots, N. \quad (3)$$

The Chebyshev collocation points result from a simple change of variables, which relates the Chebyshev interpolation series to a Fourier cosine series [39]. To evaluate the \hat{Q}_n , the inverse relation is required. This is

$$\hat{Q}_n = \hat{c}_n \sum_{l=0}^N w_l B_n(x_l) Q_l, \quad n = 0, 1, \dots, N, \quad (4)$$

with w_l being a normalized weighting function and \hat{c}_n a constant. These variables assume the following expressions to a Chebyshev-Gauss-Lobatto interpolation:

$$\hat{c}_n = \frac{2}{N\bar{c}_n}, \quad \text{where: } \bar{c}_n = \begin{cases} 2, & n = 0 \text{ or } N \\ 1, & 1 < n < N-1 \end{cases}; \text{ and } w_l = \frac{1}{\bar{c}_l}. \quad (5)$$

Legendre collocation is based on using Legendre polynomials as the basis function in Eq. (1), e.g.,

$$B_n(x) = [(2n-1)xP_{n-1}(x) - (n-1)P_{n-2}(x)]/n, \quad n \geq 2, \quad (6)$$

where: $P_0(x) = 1$ and $P_1(x) = x$. Interpolation via Legendre series cannot easily be related to trigonometric interpolation, so there is no simple expression to evaluate the \hat{Q}_n coefficients. Appeal must be made to the theory of numerical quadrature to form an approximation to the integrals which result from analytic Legendre



interpolation [40]. Considering Eq. (4), the normalized weights and constant of the Legendre-Gauss-Lobatto collocation points are

$$w_1 = \frac{1}{N(N+1)B_N^2(x_1)} \text{ and } \hat{c}_n = \begin{cases} 2n+1, & n = 0, 1, \dots, N-1 \\ N, & n = N \end{cases} \quad (7)$$

In this work, it was assumed that the Legendre-Gauss-Lobatto collocation points are the same as the Chebyshev-Gauss-Lobatto ones. It was also adopted the following collocation points and normalized weight for the Chebyshev-Gauss-Radau interpolation, based on the work of [41]:

$$x_1 = \cos\left(\frac{2\pi l}{2N+1}\right), \quad (8)$$

$$w_1 = \begin{cases} \frac{N}{2N+1}, & l = 0 \\ \frac{N}{N+1}, & \text{elsewhere} \end{cases} \quad (9)$$

For the Legendre-Gauss-Radau interpolation, also based in [41], the collocation points are defined by Eq. (8) and the normalized weights are described by:

$$w_1 = \begin{cases} \frac{1}{(N+1)^2}, & l = 0 \\ \frac{1}{2(N+1)^2} \times \frac{1-x_1}{B_N(x_1)}, & \text{elsewhere} \end{cases} \quad (10)$$

The same calculation to the vector of conserved variables Q is applied to the vector of flux C , to be defined in section 4.

Hence, we have two collocation point options and two normalized weight functions to be considered by the Chebyshev and the Legendre methods, namely: Chebyshev-Gauss-Radau, Chebyshev-Gauss-Lobatto, Legendre-Gauss-Radau and Legendre-Gauss-Lobatto.

3. Reactive Euler and Navier-Stokes Equations in 2D

As the Navier-Stokes equations tend to the Euler equations when high Reynolds number are employed, only the former equations are presented. The reactive Navier-Stokes equations in thermochemical non-equilibrium, where the rotational and vibrational contributions are considered, were implemented on conservative and finite volume contexts, in the two-dimensional space. In this case, these equations in integral and conservative forms can be expressed by:

$$\frac{\partial}{\partial t} \int_V Q dV + \int_S \vec{F} \cdot \vec{n} dS = \int_V S_{CV} dV, \text{ with: } \vec{F} = (E_e - E_v)\vec{i} + (F_e - F_v)\vec{j}, \quad (11)$$

where: Q is the vector of conserved variables, V is the volume of a computational cell, \vec{F} is the complete flux vector, \vec{n} is the unity vector normal to the flux face, S is the flux area, S_{CV} is the chemical and vibrational source term, E_e and F_e are the convective flux vectors or the Euler flux vectors in the x and y directions, respectively, and E_v and F_v are the viscous flux vectors in the x and y directions, respectively. The \vec{i} and \vec{j} unity vectors define the Cartesian coordinate system. Nine (9) conservation equations are solved: one of general mass conservation, two of linear momentum conservation, one of total energy, four of species mass conservation, and one of the vibrational internal energy of the molecules. Therefore, one of the species is absent of the iterative process. The CFD literature recommends that the species of biggest mass fraction of the gaseous mixture should be omitted, aiming to result in a minor numerical accumulation error. To the present study, in which is chosen a chemical model to the air composed of five (5) chemical species (N , O , N_2 , O_2 , and NO) and seventeen chemical reactions to the [38] model, this species can be the N_2 or the O_2 . To this work, the N_2 was chosen. The vectors Q , E_e , F_e , E_v , F_v , and S_{CV} can, hence, be defined as follows:



$$Q = \begin{Bmatrix} \rho \\ \rho u \\ \rho v \\ e \\ \rho_1 \\ \rho_2 \\ \rho_4 \\ \rho_5 \\ \rho e_v \end{Bmatrix}, E_e = \begin{Bmatrix} \rho u \\ \rho u^2 + p \\ \rho uv \\ \rho Hu \\ \rho_1 u \\ \rho_2 u \\ \rho_4 u \\ \rho_5 u \\ \rho e_v u \end{Bmatrix}, F_e = \begin{Bmatrix} \rho v \\ \rho uv \\ \rho v^2 + p \\ \rho Hv \\ \rho_1 v \\ \rho_2 v \\ \rho_4 v \\ \rho_5 v \\ \rho e_v v \end{Bmatrix}, E_v = \frac{1}{Re} \begin{Bmatrix} 0 \\ \tau_{xx} \\ \tau_{xy} \\ f_x - \phi_x \\ -\rho_1 v_{1x} \\ -\rho_2 v_{2x} \\ -\rho_4 v_{4x} \\ -\rho_5 v_{5x} \\ q_{v,x} - \phi_{v,x} \end{Bmatrix}, F_v = \frac{1}{Re} \begin{Bmatrix} 0 \\ \tau_{xy} \\ \tau_{yy} \\ f_y - \phi_y \\ -\rho_1 v_{1y} \\ -\rho_2 v_{2y} \\ -\rho_4 v_{4y} \\ -\rho_5 v_{5y} \\ q_{v,y} - \phi_{v,y} \end{Bmatrix}; \quad (12)$$

$$S_{CV} = \left\{ 0 \quad 0 \quad 0 \quad 0 \quad \dot{\omega}_1 \quad \dot{\omega}_2 \quad \dot{\omega}_4 \quad \dot{\omega}_5 \quad \sum_{s=\text{mol}} \rho_s (e_{v,s}^* - e_{v,s}) / \tau_s + \sum_{s=\text{mol}} \dot{\omega}_s e_{v,s} \right\}^T; \quad (13)$$

in which: ρ is the mixture density; u and v are Cartesian components of the velocity vector in the x and y directions, respectively; e is the fluid total energy; H is the total enthalpy; ρ_1 , ρ_2 , ρ_4 , and ρ_5 are densities of the N, O, O₂, and NO, respectively; e_v is the sum of the vibrational energy of the molecules; the τ 's are the components of the viscous stress tensor; f_x and f_y are viscous work and Fourier heat flux functions; $\rho_s v_{sx}$ and $\rho_s v_{sy}$ represent the species diffusion flux, defined by the Fick law; ϕ_x and ϕ_y are the terms of mixture diffusion; $\phi_{v,x}$ and $\phi_{v,y}$ are the terms of molecular diffusion calculated at the vibrational temperature; $\dot{\omega}_s$ is the chemical source term of each species equation, defined by the law of mass action; e_v^* is the molecular-vibrational-internal energy calculated with the translational/rotational temperature; τ_s is the translational-vibrational characteristic relaxation time of each molecule; $q_{v,x}$ and $q_{v,y}$ are the vibrational Fourier heat flux components in the x and y directions, respectively; and Re is the laminar Reynolds number.

The viscous stresses, in N/m², are determined, according to a Newtonian fluid model, by:

$$\begin{aligned} \tau_{xx} &= [2\mu_m \partial u / \partial x - 2/3 \mu_m (\partial u / \partial x + \partial v / \partial y)]; \\ \tau_{xy} &= \mu_m (\partial u / \partial y + \partial v / \partial x); \\ \tau_{yy} &= [2\mu_m (\partial v / \partial y) - 2/3 \mu_m (\partial u / \partial x + \partial v / \partial y)], \end{aligned} \quad (14)$$

where μ_m is the molecular viscosity. Expressions to f_x and f_y are given below:

$$f_x = \tau_{xx} u + \tau_{xy} v + q_x + q_{v,x}; \quad (15)$$

$$f_y = \tau_{xy} u + \tau_{yy} v + q_y + q_{v,y}, \quad (16)$$

where q_x and q_y are the Fourier heat flux components and are given by:

$$q_x = k \frac{\partial T}{\partial x} \text{ and } q_y = k \frac{\partial T}{\partial y}. \quad (17)$$

where: k is the thermal conductivity due to translation and rotation. The $q_{v,x}$ and $q_{v,y}$ are the vibrational heat flux components and are given by:

$$q_{v,x} = k_v \partial T_v / \partial x \text{ and } q_{v,y} = k_v \partial T_v / \partial y, \quad (18)$$

with k_v being the vibrational thermal conductivity and T_v is the vibrational temperature, what characterizes this model as of two temperatures: translational/rotational and vibrational. The terms of species diffusion, defined by the Fick law, to a condition of thermal non-equilibrium, are determined by [42]:

$$\rho_s v_{sx} = -\rho D_s \frac{\partial Y_{MF,s}}{\partial x} \text{ and } \rho_s v_{sy} = -\rho D_s \frac{\partial Y_{MF,s}}{\partial y}, \quad (19)$$



with “s” referent to a given species, $Y_{MF,s}$ being the molar fraction of the species, defined as:

$$Y_{MF,s} = \frac{\rho_s / M_s}{\sum_{k=1}^{ns} \rho_k / M_k} \quad (20)$$

and D_s is the species-effective-diffusion coefficient. “ns” is the number of species. The diffusion terms ϕ_x and ϕ_y which appear in the energy equation are defined by [38]:

$$\phi_x = \sum_{s=1}^{ns} \rho_s v_{sx} h_s \text{ and } \phi_y = \sum_{s=1}^{ns} \rho_s v_{sy} h_s, \quad (21)$$

being h_s the specific enthalpy (sensible) of the chemical species “s”. The molecular diffusion terms calculated at the vibrational temperature, $\phi_{v,x}$ and $\phi_{v,y}$, which appear in the vibrational-internal-energy equation are defined by [42]:

$$\phi_{v,x} = \sum_{s=mol} \rho_s v_{sx} h_{v,s} \text{ and } \phi_{v,y} = \sum_{s=mol} \rho_s v_{sy} h_{v,s}, \quad (22)$$

With $h_{v,s}$ being the specific enthalpy (sensible) of the chemical species “s” calculated at the vibrational temperature T_v . The sum of Eq. (13), as also those present in Eq. (22), considers only the molecules of the system, namely: N_2 , O_2 , and NO . The laminar Reynolds number is estimated by:

$$Re = \frac{\rho_{char} V_{initial} L_{char}}{\mu_{m,char}}, \quad (23)$$

with “char” representing characteristic or freestream properties, ρ_{char} is the characteristic density, $V_{initial}$ is the initial velocity of the fluid flow, L_{char} is a characteristic configuration length, and $\mu_{m,char}$ is a characteristic molecular viscosity. For details of the chemical model, the calculation of thermodynamic and transport properties see [43-44].

4. Numerical Schemes

Considering the two-dimensional and structured case, the flux vector splitting algorithms follow that described in [34-35, 43-44]. The speed of sound is defined by the following expression:

$$a = \sqrt{(\beta + 1) \frac{p}{\rho}}, \quad (24)$$

where β is a parameter to be defined, calculated at each interaction.

The system is solved in three parts separately, according to [45]. The first part takes into account the dynamic part, which considers the Navier-Stokes equations, the second one takes into account the chemical part involving the chemical contributions, and finally, the third part considers only the vibrational contribution. Hence, the discrete-dynamic-convective flux, which solves the dynamic part, is given by:

$$R_m = |S|_m \left\{ \frac{1}{2} M_m \left[\begin{array}{c} (\rho a) \\ (\rho a u) \\ (\rho a v) \\ (\rho a H)_L \end{array} \right] + \begin{array}{c} (\rho a) \\ (\rho a u) \\ (\rho a v) \\ (\rho a H)_R \end{array} \right] - \frac{1}{2} \phi_m \left[\begin{array}{c} (\rho a) \\ (\rho a u) \\ (\rho a v) \\ (\rho a H)_R \end{array} \right] - \begin{array}{c} (\rho a) \\ (\rho a u) \\ (\rho a v) \\ (\rho a H)_L \end{array} \right] \left. \right\} + \begin{array}{c} 0 \\ S_x p \\ S_y p \\ 0 \end{array} \Big|_m, \quad (25)$$

where $m = 1, 2, 3$ representing each one a cell interface, “R” being the cell “i” and “L” being its neighbor; the discrete-chemical-convective flux is defined by:

$$R_m = |S|_m \left\{ \frac{1}{2} M_m \left[\begin{array}{c} (\rho_1 a) \\ (\rho_2 a) \\ (\rho_4 a) \\ (\rho_5 a)_L \end{array} \right] + \begin{array}{c} (\rho_1 a) \\ (\rho_2 a) \\ (\rho_4 a) \\ (\rho_5 a)_R \end{array} \right] - \frac{1}{2} \phi_m \left[\begin{array}{c} (\rho_1 a) \\ (\rho_2 a) \\ (\rho_4 a) \\ (\rho_5 a)_R \end{array} \right] - \begin{array}{c} (\rho_1 a) \\ (\rho_2 a) \\ (\rho_4 a) \\ (\rho_5 a)_L \end{array} \right] \left. \right\}, \quad (26)$$



and finally the discrete-vibrational-convective flux is given by:

$$\mathbf{R}_m = |\mathbf{S}_m| \left\{ \frac{1}{2} \mathbf{M}_m [(\rho \mathbf{e}_v)_L + (\rho \mathbf{e}_v)_R] - \frac{1}{2} \phi_m [(\rho \mathbf{e}_v)_R - (\rho \mathbf{e}_v)_L] \right\}, \quad (27)$$

where: \mathbf{C} is the sum of the fluxes at each interface, and $\mathbf{S}^m = [\mathbf{S}_x \quad \mathbf{S}_y]_m^T$ defines the normal area vector for the surface “m”. The normal area components S_x and S_y to each flux interface are given by

$$\mathbf{S}_x^m = \mathbf{n}_x^m \mathbf{S}^m \text{ and } \mathbf{S}_y^m = \mathbf{n}_y^m \mathbf{S}^m. \quad (28)$$

The normal unity vector components, \mathbf{n}_x^m and \mathbf{n}_y^m , and the flux area of the “m” interface, \mathbf{S}^m , are defined as:

$$\mathbf{n}_x^m = \Delta y_m / (\Delta x_m^2 + \Delta y_m^2)^{0.5}, \quad \mathbf{n}_y^m = -\Delta x_m / (\Delta x_m^2 + \Delta y_m^2)^{0.5}, \text{ and } \mathbf{S}^m = (\Delta x_m^2 + \Delta y_m^2)^{0.5}. \quad (29)$$

Expressions to Δx_m and Δy_m are given in Tab. 1.

The same definitions presented in [34-35, 43-44] are valid to these algorithms. The definition of the dissipation term ϕ determines the particular formulation of the convective fluxes. The choice below corresponds to the [34] scheme, according to [46]:

$$\phi_m = \phi_m^{VL} = \begin{cases} |\mathbf{M}_m|, & \text{if } |\mathbf{M}_m| \geq 1; \\ |\mathbf{M}_m| + 0.5(\mathbf{M}_R - 1)^2, & \text{if } 0 \leq \mathbf{M}_m < 1; \\ |\mathbf{M}_m| + 0.5(\mathbf{M}_L + 1)^2, & \text{if } -1 < \mathbf{M}_m \leq 0. \end{cases} \quad (30)$$

and the [35] scheme is obtained by, according to [46]:

$$\phi_m = \phi_m^{LS} = |\mathbf{M}_m|. \quad (31)$$

Both schemes are first-order accurate in space and in time. The high-order spatial accuracy is obtained, in the current study, by the spectral method.

The viscous formulation follows that of [47], which adopts the Green theorem to calculate primitive variable gradients. The viscous gradients at the flux interfaces are obtained by arithmetical average between cell “i” and its neighbors. As was done with the convective terms, there is a need to separate the viscous flux in three parts: dynamic viscous flux, chemical viscous flux, and vibrational viscous flux. The dynamic part corresponds to the first four equations of the Navier-Stokes, the chemical part corresponds to the four equations immediately below the energy equation, and the vibrational part corresponds to the equation that follows the last chemical one. The resultant ordinary differential equation system can be written as:

$$\mathbf{V}_i \, d\mathbf{Q}_i / dt = -(\mathbf{R}_1 + \mathbf{R}_2 + \mathbf{R}_3)_i = -\mathbf{C}_i, \quad (32)$$

where the cell volume on an unstructured context is given by:

$$\mathbf{V}_i = 0.5 \left[(x_{n1}y_{n2} + y_{n1}x_{n3} + x_{n2}y_{n3}) - (x_{n3}y_{n2} + y_{n3}x_{n1} + x_{n2}y_{n1}) \right], \quad (33)$$

with $n1$, $n2$ and $n3$ being the nodes of a given triangular cell, defined in Fig. 1. Figure 1 exhibits the computational cell adopted for the simulations, as well its respective nodes, neighbors and flux interfaces.

In the present study, the Euler backward method was employed to march the scheme in time. This method is first-order accurate in time, to the three types of complete flux. To the convective dynamic component, this method can be represented in general form by:

$$\mathbf{Q}_i^{(n+1)} = \mathbf{Q}_i^{(n)} - (\Delta t_i / \mathbf{V}_i) \times \mathbf{C}(\mathbf{Q}_i^{(n)}), \quad (34)$$

to the convective chemical part, it can be represented in general form by:

$$\mathbf{Q}_i^{(n+1)} = \mathbf{Q}_i^{(n)} - \Delta t_i \times \left[\mathbf{C}(\mathbf{Q}_i^{(n)}) / \mathbf{V}_i - \mathbf{S}_C(\mathbf{Q}_i^{(n)}) \right], \quad (35)$$

where the chemical source term \mathbf{S}_C is calculated with the temperature T_{rc} (reaction rate controlling temperature, see [43-44]). Finally, to the convective vibrational component:

$$\mathbf{Q}_i^{(n+1)} = \mathbf{Q}_i^{(n)} - \Delta t_i \times \left[\mathbf{C}(\mathbf{Q}_i^{(n)}) / \mathbf{V}_i - \mathbf{S}_V(\mathbf{Q}_i^{(n)}) \right], \quad (36)$$



in which:

$$S_V = \sum_{s=\text{mol}} q_{T-V,s} + \sum_{s=\text{mol}} S_{C,s} e_{v,s}, \quad (37)$$

where q_{T-V} is the heat flux due to translational-vibrational relaxation, defined in Eq. (13) and in [43-44].

5. Spatially Variable Time Step

The spatially variable time step has proved efficient gains in terms of convergence acceleration, as verified by [36-37]. Initially, the parameter σ is determined, where:

$$\sigma_s = \frac{c_s}{M_s} \text{ and } \sigma = \sum_{s=1}^{ns} \sigma_s, \quad (38)$$

with c_s being the mass fraction, and M_s the molecular weight. The total specific heat at constant volume due to translation is defined as:

$$c_{V,T} = \sum_{s=1}^{ns} \sigma_s c_{V,T,s}, \quad (39)$$

where, for each gas constituent of the five (5) species chemical model, the specific heat at constant volume, based on the kinetic theory of gases [48], is defined by

$$c_{V,T,N} = \frac{3}{2} R_N, \quad c_{V,T,O} = \frac{3}{2} R_O, \quad c_{V,T,N_2} = \frac{5}{2} R_{N_2}, \quad c_{V,T,O_2} = \frac{5}{2} R_{O_2}, \quad \text{and } c_{V,T,NO} = \frac{5}{2} R_{NO}, \quad (40)$$

being R_s the specific gas constant. The total pressure of the gaseous mixture is determined by Dalton law, which indicates that the total pressure of the gas is the sum of the partial pressure of each constituent gas, resulting in:

$$p_s = c_s \rho R_s T \text{ and } p = \sum_{s=1}^{ns} p_s. \quad (41)$$

The speed of sound to a reactive mixture can be determined by Eq. (24), where $\beta = \frac{R_{\text{univ}} \sigma}{c_{V,T}}$, with $R_{\text{univ}} = 1.987$

cal/(g-mol.K). Finally, the spatially variable time step is defined from the CFL (Courant-Friedrichs-Lewis) definition:

$$\Delta t_i = \frac{\text{CFL} \Delta s_i}{\sqrt{u_i^2 + v_i^2} + a_i}, \quad (42)$$

where Δs_i is the characteristic length of each cell (defined between the minimum cell side length and the minimum centroid distance between each cell and its neighbors).

6. Dimensionless Scales, Initial and Boundary Conditions

6.1. Dimensionless Scales

The dimensionless scales employed to the reactive equations consisted in: R_s is dimensionless by a_{char} , where $a_{\text{char}} = \sqrt{\gamma p_{\text{char}} / \rho_{\text{char}}}$; c_v is dimensionless by a_{char} ; h_s and Δh_s^0 are dimensionless by a_{char}^2 ; T and T_v , translational/rotational temperature and vibrational temperature, respectively, are dimensionless by a_{char} ; ρ_s and ρ are dimensionless by ρ_{char} ; u and v are dimensionless by a_{char} ; μ is dimensionless by μ_{char} ; D , diffusion coefficient, dimensionless by $a_{\text{char}}^2 dt_{\text{char}}$, where dt_{char} is the minimum time step calculated in the computational domain at the first iteration; $\dot{\omega}$ is dimensionless by $(\rho_{\text{char}} / dt_{\text{char}}) \times 10^{-3}$; e_v is dimensionless by a_{char}^2 ; e and p are dimensionless by $\rho_{\text{char}} a_{\text{char}}^2$; τ_s , relaxation time, is dimensionless by dt_{char} . The characteristic physical properties are defined in [49].



6.2. Initial Condition

The initial conditions to the blunt body, and to the double ellipse problems, for a five species chemical model, are presented in Tabs. 2-3. The Reynolds number is obtained from data of [49].

6.3. Boundary Conditions

The boundary conditions are basically of three types: solid wall, entrance, and exit. These conditions are implemented with the help of ghost cells.

Wall condition. In the inviscid case, this condition imposes the flow tangency at the solid wall. This condition is satisfied considering the wall tangent velocity component of the ghost volume as equals to the respective velocity component of its real neighbor cell. At the same way, the wall normal velocity component of the ghost cell is equaled in value, but with opposite signal, to the respective velocity component of the real neighbor cell. Hence, the ghost cell velocity components are written as:

$$\mathbf{u}_g = (\mathbf{n}_y^2 - \mathbf{n}_x^2)\mathbf{u}_r - (2\mathbf{n}_x\mathbf{n}_y)\mathbf{v}_r; \quad \text{and} \quad \mathbf{v}_g = -(2\mathbf{n}_x\mathbf{n}_y)\mathbf{u}_r + (\mathbf{n}_x^2 - \mathbf{n}_y^2)\mathbf{v}_r. \quad (43)$$

with “g” related with ghost cell and “r” related with real cell. To the viscous case, the boundary condition imposes that the ghost cell velocity components be equal to the real cell velocity components, with the negative signal:

$$\mathbf{u}_g = -\mathbf{u}_r \quad \text{and} \quad \mathbf{v}_g = -\mathbf{v}_r. \quad (44)$$

The normal pressure gradient of the fluid at the wall is assumed to be equal to zero according to a boundary-layer like condition. The same hypothesis is applied for the normal temperature gradient at the wall, assuming an adiabatic wall. From the above considerations, density and translational/rotational temperature are extrapolated from the respective values of its real neighbor volume (zero order extrapolation). The total vibrational internal energy is also extrapolated.

With the mixture-species-mass fractions and with the values of the respective specific heats at constant volume, it is possible to obtain the mixture specific heat at constant volume. The mixture formation enthalpy is extrapolated from the real cell. The mixture total energy to the ghost cell is calculated by:

$$e_g = \rho_g \left[c_{v,mixt,g} (T_{tr,g} - T_{REF}) + \Delta h_{mixt,g}^0 + e_{v,g} + 0.5(u_g^2 + v_g^2) \right], \quad (45)$$

Where $c_{v,mixt,g}$, T_{REF} , $e_{v,g}$ are defined in [43-44]. To the species density, the non-catalytic condition is imposed, what corresponds to zero order extrapolation from the real cell.

Entrance condition. It is divided in two flow regimes:

(a) Subsonic flow: Three properties are specified and one extrapolated in the boundary conditions of the dynamic part of the [34-35] numerical schemes. This approach is based on information propagation analysis along characteristic directions in the calculation domain [50]. In other words, for subsonic flow, three characteristics propagate information pointing into the computational domain. Thus three flow properties must be fixed at the inlet plane. Just one characteristic line allows information to travel upstream. So, one flow variable must be extrapolated from the interior grid to the inlet boundary. The total energy was the extrapolated variable from the real neighbor volume, for the studied problems. Density and velocity components adopted values of initial flow. To the chemical part, four information propagate upstream because it is assumed that all four equations are conducted by the eigenvalue “ (q_n-a) ”. In the subsonic flow, all eigenvalues are negative and the information should be extrapolated. In the same reasoning to the chemical boundary conditions, the vibrational-internal-energy equation is dictated by the “ (q_n-a) ” eigenvalue and, in the subsonic region, its value is negative. Hence, the vibrational internal energy should be extrapolated.

(b) Supersonic flow: In this case no information travels upstream; therefore all variables are fixed with their initial values.

Exit condition. It is also divided in two flow regimes:

(a) Subsonic flow: Three characteristics propagate information outward the computational domain. Hence, the associated variables should be extrapolated from interior information. The characteristic direction associated to the “ $(q_{normal}-a)$ ” velocity should be specified because it points inward to the computational domain [50]. In this



case, the ghost volume total energy is specified from its initial value. Density and velocity components are extrapolated. To the chemical part, the eigenvalue “ (q_n-a) ” is again negative and the characteristics are always flowing into the computational domain. Hence, the four chemical species under study should have their densities fixed by their initial values. In the same reasoning, the internal vibrational energy should have its value prescribed by its initial value due to the eigenvalue “ (q_n-a) ” be negative.

(b) Supersonic flow: All variables are extrapolated from interior grid cells, as no flow information can make its way upstream. In other words, nothing can be fixed.

7. Physical Problems

Two physical problems were solved in this work, namely: blunt body, and double ellipse. The first problem considers the geometry of a blunt body with 1.0 m of nose ratio and parallel rectilinear walls. The far field is located at 20.0 times the nose ratio in relation to the configuration nose. A mesh composed of 5,096 triangular cells and 2,650 nodes was studied for the inviscid case, with an exponential stretching of 5.0% for the viscous case. This mesh is equivalent in finite differences to a one of 53x50 points. Figure 2 shows the detail of the geometry and Figs. 3 and 4 exhibit the inviscid and viscous meshes.

The double ellipse problem is the second under study. The mesh is composed of 8,232 triangular cells and 4,250 nodes, with an exponential stretching of 5.0% for the viscous case, and far field located at 20.0 unities. This mesh is equivalent in finite differences to a one of 85x50 points. Figure 5 shows the double ellipse geometry and Figs. 6 and 7 exhibit the inviscid and viscous meshes.

8. Results

Tests were performed in a Core i7 processor of 2.3GHz and 8.0Gbytes of RAM microcomputer, in a Windows 7.0 environment. Three (3) orders of reduction of the maximum residual in the field were considered to obtain a converged solution. The residual was defined as the value of the discretized conservation equation. In the dynamic part of the [34-35] schemes, such definition results in:

$$\text{Residual} = -\Delta t_i / V_i \times C_i. \quad (46)$$

The attack angle was adopted equal to zero. In this work, the inviscid results were obtained for a 5th order of accuracy of the spectral method, whereas the viscous solutions were obtained for a 8th order of accuracy of the spectral method. For a matter of simplicity, the following abbreviations were used: [34] scheme = VL, [35] scheme = LS, Chebyshev-Gauss-Radau = CGR, Chebyshev-Gauss-Lobatto = CGL, Legendre-Gauss-Radau = LGR, and Legendre-Gauss-Lobatto = LGL.

8.1. Blunt Body Problem

Inviscid case. Figures 8 to 11 exhibit the pressure and temperature contours obtained by the VL and LS schemes as using the CGR collocation points. The LS algorithm captures a more intense shock than the VL scheme, as can be seen by the pressure legend. Good homogenous properties are observed in the pressure and in the translational/rotational temperature contours. No pre-shock oscillations are observed. The maximum temperature at the configuration nose is 8,951.11K, obtained by the VL scheme.

Figures 12 to 15 show the pressure and translational/rotational temperature contours generated by the VL and LS schemes as using CGL collocation points. The maximum pressure is obtained by the LS algorithm, being inferior to that observed in the CGR case. No pressure oscillations are observed in the solutions. The temperature contours presents good homogeneous properties. The maximum temperature reaches the value of 8,986.87K and is captured by the VL scheme. The contours are free of oscillations.

Figures 16 to 19 present the pressure and translational/rotational temperature contours calculated by the VL and LS schemes when using the LGR collocation points. The pressure peaks of both solutions are smaller than those obtained in the Chebyshev variants. No pressure oscillations are observed. The maximum temperature peak is 9,027.15K, obtained again by the VL scheme. Good homogeneous properties are also observed in both temperature contours.

Figures 20 to 23 exhibit the pressure and temperature contours obtained by the VL and LS algorithms when using the LGL collocation points. The pressure peaks are still low. The shock wave is well captured by both



schemes. The temperature contours present good homogeneous properties, free of oscillations. The maximum temperature is obtained by the VL scheme with a value of 9,016.46K.

Viscous case. Figures 24 and 25 present the pressure and temperature contours generated by the LS scheme as using CGR collocation points. The VL scheme did not yield converged results. The pressure peak is closer to the theoretical stagnation pressure value. Good homogenous properties are observed and no pre-shock oscillations are observed. The maximum temperature reaches the mark of 9,025.58K. Good symmetry properties are verified in the temperature field.

Figures 26 to 29 show the pressure and translational/rotational temperature contours calculated by the VL and LS algorithms when using CGL collocation points. The VL's pressure peak is very close to the theoretical value of stagnation pressure (see Table 4). The shock wave is well captured by both schemes. Figures 28 and 29 show the translational/rotational temperature contours and the good transport of viscosity and thermal conduction is noted in the VL solution. Note that the heat transfer is better captured by the VL scheme, as can be seen by the contours of temperature close to the configuration wall. The correct transport of properties like viscosity and thermal conduction are qualitatively confirmed. The maximum temperature is 9,205.91K and is again obtained by the VL scheme; in other words, the VL scheme is being more conservative than the LS scheme.

Figures 30 to 33 exhibit the pressure and temperature contours obtained by the VL and LS algorithms as using the LGR collocation points. Both pressure contours are very similar in qualitative terms, although the pressure peaks are very low. Good symmetry properties are observed in both solutions, free of pre-shock oscillations. Figures 32 and 33 exhibit the temperature contours calculated by the VL and LS schemes. The temperature field of VL algorithm is more intense than that of the LS scheme, reaching a maximum of 9,195.82K. Good symmetry and homogenous properties are observed in both figures.

Figures 34 to 37 present the pressure and translational/rotational temperature contours calculated by the VL and LS algorithms when using the LGL collocation points. Both pressures are reduced in relation to the theoretical stagnation pressure value. Both solutions present good symmetry and homogenous properties, free of oscillations. The shock waves are well captured and the transport of properties is well highlighted in the VL's temperature contours. The maximum temperature is obtained by the VL scheme and reaches the value of 9,200.61K. The Legendre solutions present in general higher values to the stagnation temperature than the Chebyshev solutions. In general terms, the Chebyshev variants dominate the pressure field, whereas the Legendre variants dominate the temperature field.

8.2. Double Ellipse Problem

Inviscid case. In this problem, only the VL scheme converged in the numerical simulations. Figures 38 to 45 show pressure and temperature contours generated by the VL algorithm as using the CGR, CGL, LGR, and LGL collocation points. Comparing with the theoretical stagnation pressure value, the best result is due to CGR collocation points with an error of 0.09%. Good homogenous properties are observed in all solutions and the two shock waves are well captured by all spectral variants. The maximum temperature in the field is captured by the LGL collocation points and reaches the value of 10,112.70K.

Viscous case. Again, only the VL scheme generated converged results and the CGR collocation points did not present solutions. Figures 46 to 51 exhibit the pressure and temperature contours calculated with the VL scheme as using the CGL, LGR, and LGL variants of the proposed spectral method. The best value to the stagnation pressure is captured by the CGL collocation points, with an error of 1.65%. Good homogenous properties are observed in all solutions. Figures 47, 49, and 51 exhibit the thermal boundary layer captured by all variants of the spectral method as using the VL scheme. The transport properties are well detected by the VL scheme. No temperature oscillations are observed in these figures. The temperature fields calculated by the Legendre variants reach values above 10,400K and are the most intense fields in the double ellipse simulations.

8.3. Other Comparisons

Figure 52 shows the convergence history of the VL scheme to a 5th order spectral method using LGL collocation points and to a structured MUSCL solution of 2nd order using the minmod limiter, for the blunt body inviscid case. The LGL collocation points were chosen because they provide the best convergence of the VL scheme for



the inviscid case and 5th order of accuracy. The structured MUSCL procedure was implemented by the author and was used for numerical comparisons due to its moderate CFL number in the blunt body simulations. To details of the implementation of the structured MUSCL procedure on a context of thermochemical non-equilibrium, the reader is encouraged to read [51]. As can be seen in Fig. 52, the spectral (LGL) method coupled with the VL scheme was the most efficient converging in 1,344 iterations, with a maximum CFL of 0.10. The MUSCL solution was very inefficient compared with the spectral method. The maximum allowable CFL number employed in the MUSCL solution was 0.10. Figure 53 compares the structured MUSCL solution of 2nd order and the spectral (LGL) method, all of them coupled with the LS scheme. Again, the LGL collocation points were chosen due to provide the best convergence for the LS scheme in the inviscid case and 5th order of accuracy. In this case, the good convergence of the spectral (LGL) method was highlighted, converging in 523 iterations, whereas the MUSCL solutions converged in more than 2,000 iterations.

As conclusion, the correct implementation of the proposed spectral method on an unstructured context led to an efficient high order scheme, converging in less than 1,500 iterations in the inviscid case, for the blunt body problem, when programmed coupled with the VL or LS schemes. The LGL variant of the spectral method was the most efficient in the studies performed by this author and ratified the fast convergence as expected.

8.4. Quantitative Analysis

In order to perform a quantitative analysis, the present reactive results are compared to the perfect gas solutions. The stagnation pressures at the blunt body nose, and at the double ellipse nose were evaluated assuming the perfect gas formulation. Such parameter calculated at this way is not the best comparison, but in the absence of practical reactive results, this constitutes the best available solution.

To calculate the stagnation pressure at the nose of these two configurations, [52] presents in its B Appendix values of the normal shock wave properties ahead of the configuration. The ratio pr_0/pr_∞ is estimated as function of the normal Mach number and the stagnation pressure pr_0 can be determined from this parameter. Hence, Table 4 gives the theoretical stagnation pressure values obtained for the two configurations at the initial-normal-Mach number. The value of pr_∞ is determined by the following expression:

$$pr_\infty = \frac{Pr_{\text{initial}}}{\rho_{\text{char}} \times a_{\text{char}}^2}, \quad (47)$$

where, for example, for the blunt body case, $pr_{\text{initial}} = 687\text{N/m}^2$, $\rho_{\text{char}} = 0.004\text{kg/m}^3$ and $a_{\text{char}} = 317.024\text{m/s}$. Considering these values, one concludes that $pr_\infty = 1.709$ (non-dimensional). Using the ratio obtained from [52], the stagnation pressure ahead of the configuration nose is estimated as 170.87 unities. Tables 5 (inviscid case) and 6 (viscous case) compare values of the stagnation pressure obtained from the simulations with the theoretical values and show the percentage errors. As can be seen, the best results in the inviscid case are provided by the CGR collocation points, with an error of 3.85%, when coupled with the VL scheme, for the blunt body problem; and again by the CGR collocation points, with an error of 0.09%, when coupled with the VL scheme, for the double ellipse problem. For the viscous case, the CGL collocation points, with an error of 1.65%, coupled with the VL scheme, for the blunt body problem, was the best; and with the CGL collocation points, with an error of 2.17%, coupled with the VL scheme, for the double ellipse problem, was the best.

As the hypersonic flow around the blunt body configuration was simulated with a zero value to the attack angle, a zero lift coefficient, due to geometry symmetry, is the expected value for this aerodynamic coefficient. Table 7 presents an analysis of the lift aerodynamic coefficient, based only on pressure contribution, for both inviscid and viscous cases in this study. As can be observed, the best value to the lift coefficient in the inviscid case is obtained by the LGL collocation points, coupled with the LS scheme, for the blunt body problem. In the viscous case, the best value to the lift coefficient is obtained by the CGL collocation points, coupled with the LS scheme, for the blunt body problem.

8.5. Computational Performance

Tables 8 and 9 present the computational data of the VL and LS schemes for the blunt body, and for the double ellipse problems in both inviscid and viscous cases. It shows the CFL number and the number of iterations to



convergence for all studied cases in the current work. It can be verified that the best performance of the VL scheme in the inviscid case occurred when using the LGL collocation points, employing a CFL of 0.10, and converging in 1,344 iterations, in the blunt body problem, whereas in the viscous case occurred when using the LGL collocation points, employing a CFL of 0.08, and converging in 2,713 iterations, also in the blunt body problem. On the other hand, the best performance of the LS scheme in the inviscid case occurred when using the LGL collocation points, employing a CFL of 0.20, and converging in 523 iterations, in the blunt body problem, whereas in the viscous case occurred when using the LGR collocation points, employing a CFL of 0.20, and converging in 1,074 iterations, also in the blunt body problem.

As final conclusion, it is possible to highlight that, for the blunt body problem, the VL scheme in the viscous case using CGL collocation points had the best performance in estimating the stagnation pressure, and the lift aerodynamic coefficient was best estimated by the LS scheme as using the CGL collocation points; and for the double ellipse problem, the VL scheme in the inviscid case using CGR collocation points had the best performance in estimating the stagnation pressure. Moreover, the best performance of the numerical schemes, for the 5th order of accuracy, was due to the LS one, when using the LGL collocation points, employing a CFL of 0.20, and converging in 523 iterations, in the blunt body problem, whereas for the 8th order of accuracy, the best performance of the numerical schemes was due to the LS one, when using the LGR collocation points, employing a CFL of 0.20, and converging in 1,074 iterations, also in the blunt body problem.

Finally, to close this work, the computational cost of the numerical schemes using the several types of collocation points is presented in Tab. 10. For the inviscid case, the cheapest combination was the VL scheme using CGR collocation points with a cost of 0.0001115 sec/per-volume/per-iteration, whereas for the viscous case the cheapest was due to the LS scheme coupled with the CGR collocation points with a cost of 0.0002139 sec/per-volume/per-iteration.

Table 1: Values of Δx_m and Δy_m

Interface	Δx_m	Δy_m
m = 1	$x_{n2} - x_{n1}$	$y_{n2} - y_{n1}$
m = 2	$x_{n3} - x_{n2}$	$y_{n3} - y_{n2}$
m = 3	$x_{n1} - x_{n3}$	$y_{n1} - y_{n3}$

Table 2: Initial conditions to the blunt body problem

Property	Value
M_{initial}	8.78
ρ_{initial}	0.00326 kg/m ³
p_{initial}	687 Pa
U_{initial}	4,776 m/s
T_{initial}	694 K
Altitude	40,000 m
c_N	10 ⁻⁹
c_O	0.07955
c_{O_2}	0.13400
c_{NO}	0.05090
L_{char}	2.0 m
Re_{char}	2.386x10 ⁶

Table 3: Initial conditions to the double ellipse problem

Property	Value
M_{initial}	15.0
ρ_{initial}	0.00922 kg/m ³
p_{initial}	794 Pa



U_{initial}	5,208 m/s
T_{initial}	300 K
Altitude	50,000 m
c_N	10^{-9}
c_O	0.07955
c_{O_2}	0.13400
c_{NO}	0.05090
L_{char}	5.0 m
Re_{char}	1.574×10^6

Table 4: Values of theoretical stagnation pressure

Problem:	M_{initial} :	pr_0/pr_{∞} :	pr_{∞} :	pr_0 (Theoretical):
Blunt body	8.78	99.98	1.709	170.87
Double ellipse	15.00	290.20	7.109	2,063.03

Table 5: Values of stagnation pressure and respective errors (Inviscid case/5th Order)

Physical Problem:	Scheme:	Spectral Method:	pr_0 : (Numerical)	Error:
Blunt Body ($pr_0 = 170.87$)	VL ⁽¹⁾	Chebyshev-Gauss-Radau	164.29	3.85
	LS ⁽²⁾	Chebyshev-Gauss-Radau	179.14	4.84
	VL	Chebyshev-Gauss-Lobatto	143.02	16.30
	LS	Chebyshev-Gauss-Lobatto	162.73	4.76
	VL	Legendre-Gauss-Radau	111.57	34.70
	LS	Legendre-Gauss-Radau	141.13	17.41
	VL	Legendre-Gauss-Lobatto	99.62	41.70
	LS	Legendre-Gauss-Lobatto	133.95	21.61
	VL	Chebyshev-Gauss-Radau	2,061.23	0.09
	LS	Chebyshev-Gauss-Radau	-	-
Double Ellipse ($pr_0 = 2,063.03$)	VL	Chebyshev-Gauss-Lobatto	1,842.56	10.69
	LS	Chebyshev-Gauss-Lobatto	-	-
	VL	Legendre-Gauss-Radau	1,576.21	23.60
	LS	Legendre-Gauss-Radau	-	-
	VL	Legendre-Gauss-Lobatto	1,483.22	28.10
	LS	Legendre-Gauss-Lobatto	-	-

(1): Van Leer; (2): Liou and Steffen Jr.

Table 6: Values of stagnation pressure and respective errors (Viscous case/8th Order)

Physical Problem:	Scheme:	Spectral Method:	pr_0 : (Numerical)	Error:
Blunt Body ($pr_0 = 170.87$)	VL	Chebyshev-Gauss-Radau	-	-
	LS	Chebyshev-Gauss-Radau	185.91	8.80
	VL	Chebyshev-Gauss-Lobatto	173.69	1.65
	LS	Chebyshev-Gauss-Lobatto	177.21	3.71
	VL	Legendre-Gauss-Radau	136.57	20.07
	LS	Legendre-Gauss-Radau	145.20	15.02
	VL	Legendre-Gauss-Lobatto	137.41	19.58
	LS	Legendre-Gauss-Lobatto	146.92	14.02
	VL	Chebyshev-Gauss-Radau	-	-
	LS	Chebyshev-Gauss-Radau	-	-



Double Ellipse ($pr_0 = 2,063.03$)	VL	Chebyshev-Gauss-Lobatto	2,018.33	2.17
	LS	Chebyshev-Gauss-Lobatto	-	-
	VL	Legendre-Gauss-Radau	1,591.21	22.87
	LS	Legendre-Gauss-Radau	-	-
	VL	Legendre-Gauss-Lobatto	1,602.16	22.34
	LS	Legendre-Gauss-Lobatto	-	-

Table 7: Values of the lift coefficient for the blunt body problem

Type of Flow:	Scheme:	Spectral Method:	c_L :
Inviscid case (5 th order)	VL	Chebyshev-Gauss-Radau	-5.5503×10^{-2}
	LS	Chebyshev-Gauss-Radau	-2.7735×10^{-2}
	VL	Chebyshev-Gauss-Lobatto	-4.4128×10^{-2}
	LS	Chebyshev-Gauss-Lobatto	-2.2701×10^{-2}
	VL	Legendre-Gauss-Radau	-9.3822×10^{-2}
	LS	Legendre-Gauss-Radau	-1.5975×10^{-2}
	VL	Legendre-Gauss-Lobatto	-8.8020×10^{-2}
	LS	Legendre-Gauss-Lobatto	-1.4321×10^{-2}
	VL	Chebyshev-Gauss-Radau	-
	LS	Chebyshev-Gauss-Radau	-4.4204×10^{-3}
Viscous case (8 th order)	VL	Chebyshev-Gauss-Lobatto	-2.3363×10^{-2}
	LS	Chebyshev-Gauss-Lobatto	5.6692×10^{-4}
	VL	Legendre-Gauss-Radau	-4.2447×10^{-2}
	LS	Legendre-Gauss-Radau	3.6571×10^{-3}
	VL	Legendre-Gauss-Lobatto	-4.2857×10^{-2}
	LS	Legendre-Gauss-Lobatto	3.5594×10^{-3}

Table 8: Computational data (Inviscid case/5th Order)

Physical Problem:	Scheme:	Spectral Method:	CFL:	Iterations:
Blunt Body	VL	Chebyshev-Gauss-Radau	0.10	2,483
	LS	Chebyshev-Gauss-Radau	0.10	2,646
	VL	Chebyshev-Gauss-Lobatto	0.10	1,841
	LS	Chebyshev-Gauss-Lobatto	0.40	556
	VL	Legendre-Gauss-Radau	0.10	1,426
	LS	Legendre-Gauss-Radau	0.20	623
	VL	Legendre-Gauss-Lobatto	0.10	1,344
	LS	Legendre-Gauss-Lobatto	0.20	523
	VL	Chebyshev-Gauss-Radau	0.10	4,538
	LS	Chebyshev-Gauss-Radau	-	-
Double Ellipse	VL	Chebyshev-Gauss-Lobatto	0.10	3,283
	LS	Chebyshev-Gauss-Lobatto	-	-
	VL	Legendre-Gauss-Radau	0.10	2,236
	LS	Legendre-Gauss-Radau	-	-
	VL	Legendre-Gauss-Lobatto	0.10	1,897
	LS	Legendre-Gauss-Lobatto	-	-

Table 9: Computational data (Viscous case/8th Order)

Physical Problem:	Scheme:	Spectral Method:	CFL:	Iterations:
	VL	Chebyshev-Gauss-Radau	-	-
	LS	Chebyshev-Gauss-Radau	0.10	4,963



Blunt Body	VL	Chebyshev-Gauss-Lobatto	0.10	3,879
	LS	Chebyshev-Gauss-Lobatto	0.30	1,818
	VL	Legendre-Gauss-Radau	0.08	2,750
	LS	Legendre-Gauss-Radau	0.20	1,074
	VL	Legendre-Gauss-Lobatto	0.08	2,713
	LS	Legendre-Gauss-Lobatto	0.20	1,093
	VL	Chebyshev-Gauss-Radau	-	-
	LS	Chebyshev-Gauss-Radau	-	-
Double Ellipse	VL	Chebyshev-Gauss-Lobatto	0.08	7,395
	LS	Chebyshev-Gauss-Lobatto	-	-
	VL	Legendre-Gauss-Radau	0.06	4,694
	LS	Legendre-Gauss-Radau	-	-
	VL	Legendre-Gauss-Lobatto	0.06	4,904
	LS	Legendre-Gauss-Lobatto	-	-

Table 10: Computational cost of spectral variants

Order of Accuracy:	Scheme:	Spectral Method:	Computational Cost (seconds/volumes/iterations):
5 th Order (Inviscid case)	VL	Chebyshev-Gauss-Radau	0.0001115
	LS	Chebyshev-Gauss-Radau	0.0001233
	VL	Chebyshev-Gauss-Lobatto	0.0001365
	LS	Chebyshev-Gauss-Lobatto	0.0001359
	VL	Legendre-Gauss-Radau	0.0001355
	LS	Legendre-Gauss-Radau	0.0001354
	VL	Legendre-Gauss-Lobatto	0.0001348
	LS	Legendre-Gauss-Lobatto	0.0001347
8 th Order (Viscous case)	VL	Chebyshev-Gauss-Radau	-
	LS	Chebyshev-Gauss-Radau	0.0002139
	VL	Chebyshev-Gauss-Lobatto	0.0002743
	LS	Chebyshev-Gauss-Lobatto	0.0002741
	VL	Legendre-Gauss-Radau	0.0002764
	LS	Legendre-Gauss-Radau	0.0002761
	VL	Legendre-Gauss-Lobatto	0.0002769
	LS	Legendre-Gauss-Lobatto	0.0002765

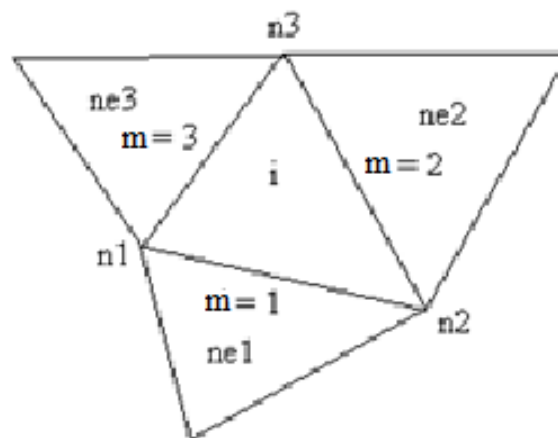


Figure 1: Schematic of a cell and its neighbors, nodes and flux interfaces



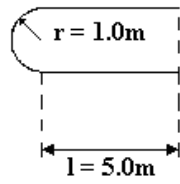


Figure 2: Blunt body configuration

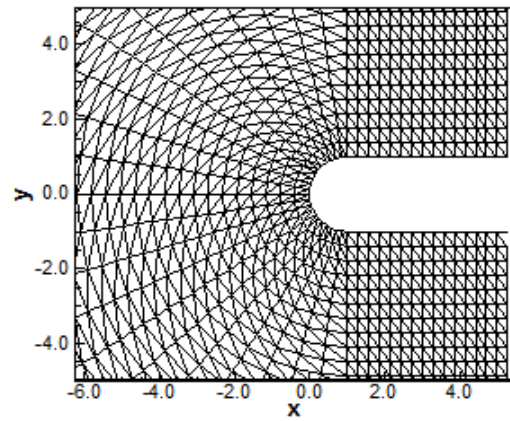


Figure 3: Blunt body inviscid mesh

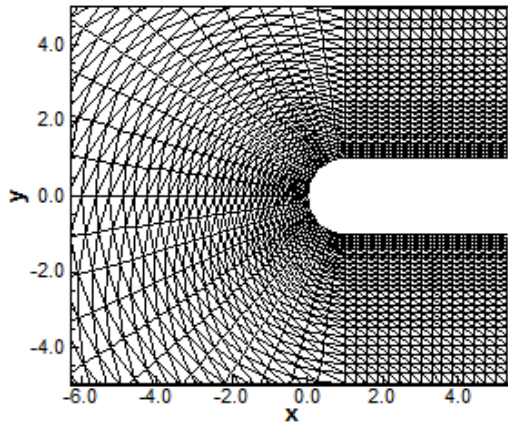


Figure 4: Blunt body viscous mesh

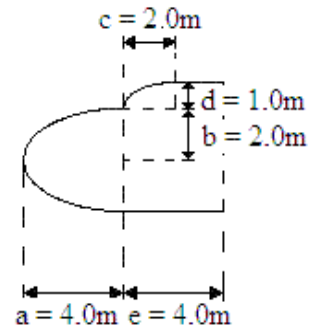


Figure 5: Double ellipse configuration

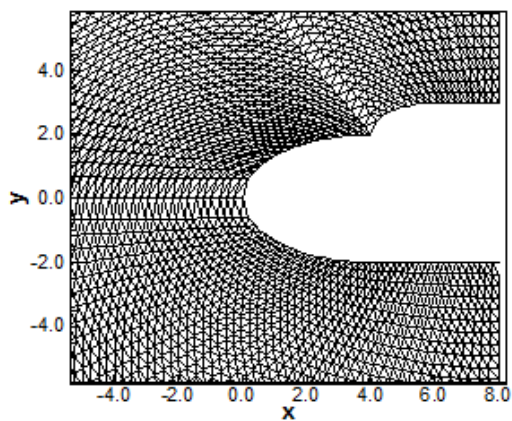


Figure 6: Double ellipse inviscid mesh.

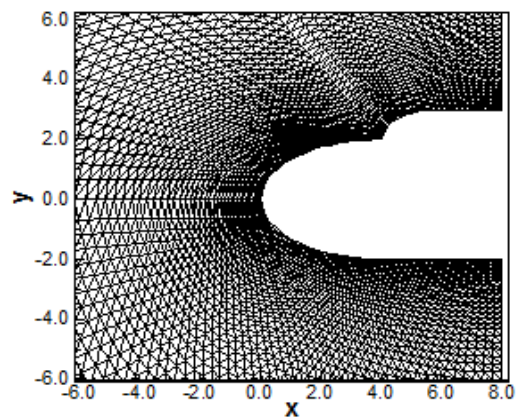


Figure 7: Double ellipse viscous mesh

Blunt Body Inviscid Solutions

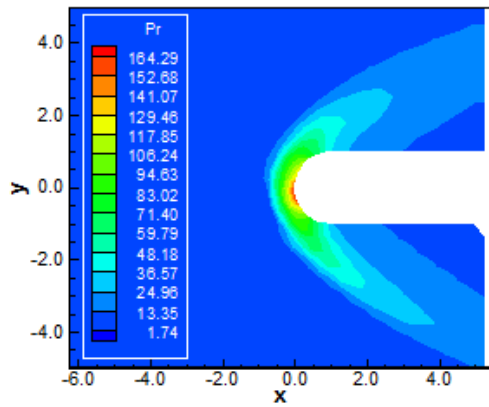


Figure 8: Pressure contours (CGR-VL)

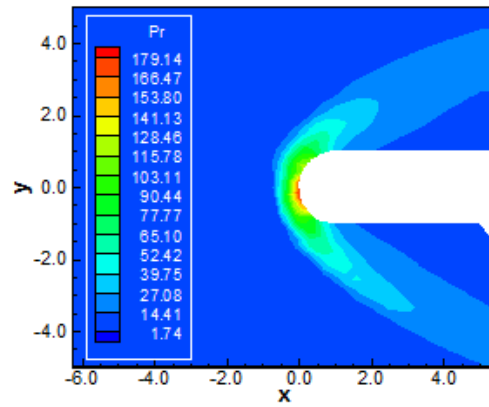


Figure 9: Pressure contours (CGR-LS)

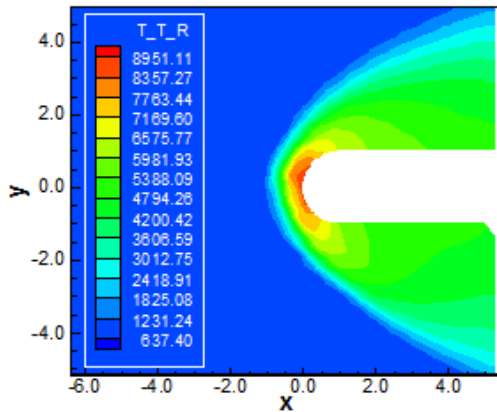


Figure 10: Translational/rotational temperature contours (CGR-VL)

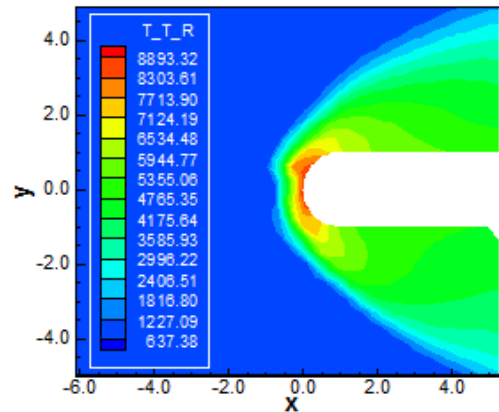


Figure 11: Translational/rotational temperature contours (CGR-LS)

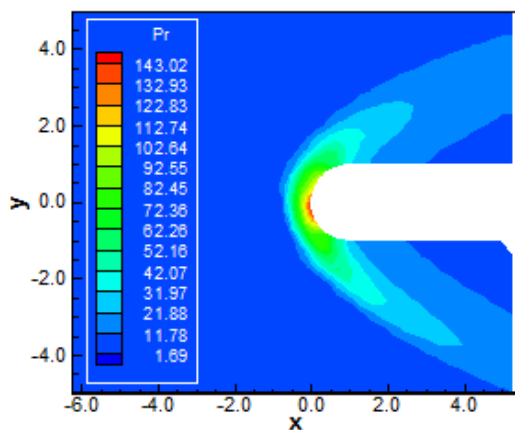


Figure 12: Pressure contours (CGL-VL)

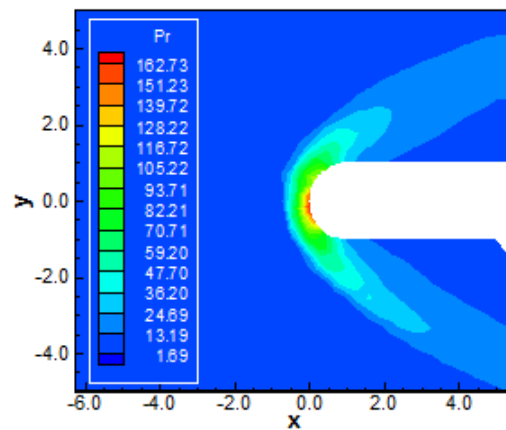


Figure 13: Pressure contours (CGL-LS)

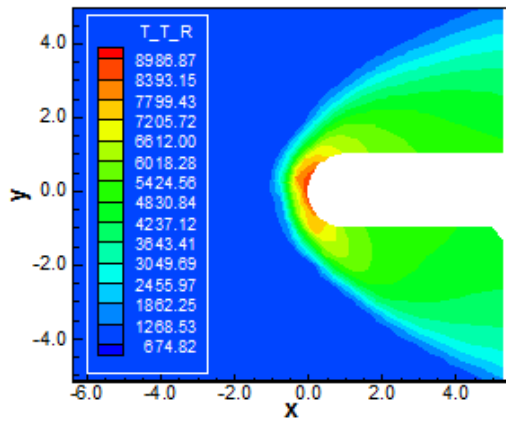


Figure 14: Translational/rotational temperature contours (CGL-VL)

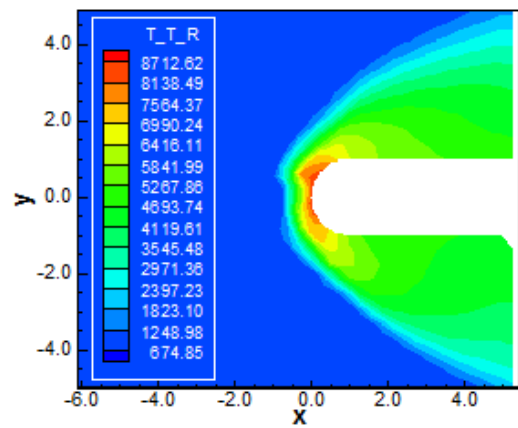


Figure 15: Translational/rotational temperature contours (CGL-LS)

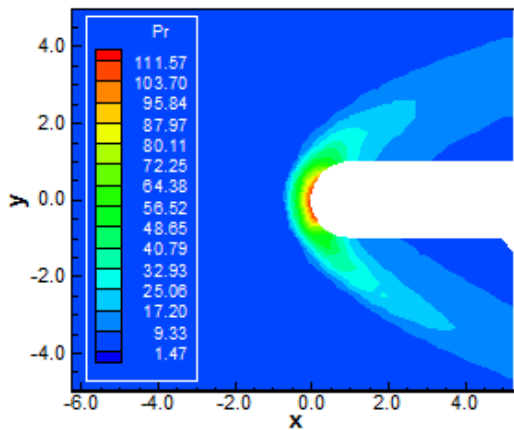


Figure 16: Pressure contours (LGR-VL)

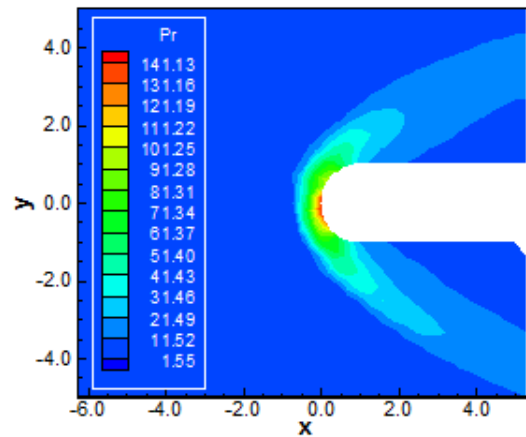


Figure 17: Pressure contours (LGR-LS)

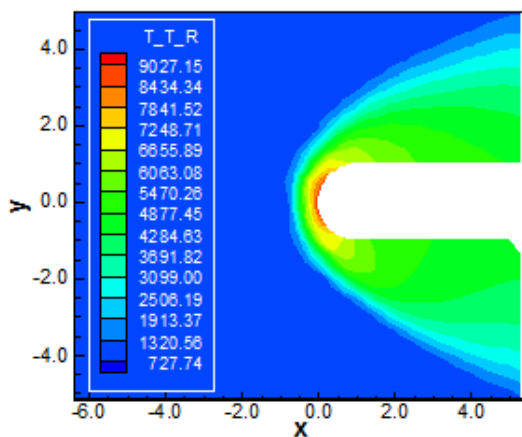


Figure 18: Translational/rotational temperature contours (LGR-VL)

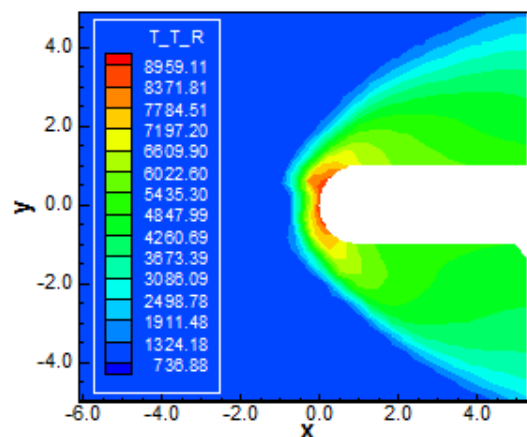


Figure 19: Translational/rotational temperature contours (LGR-LS)



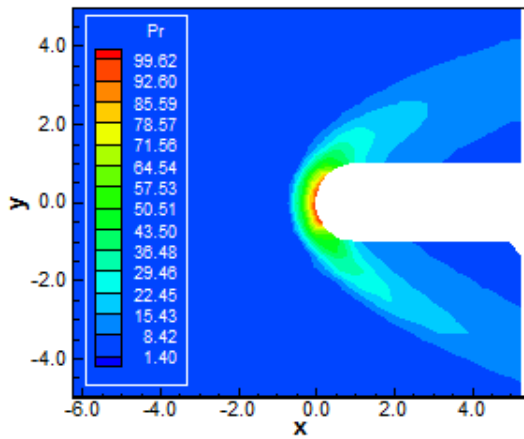


Figure 20: Pressure contours (LGL-VL)

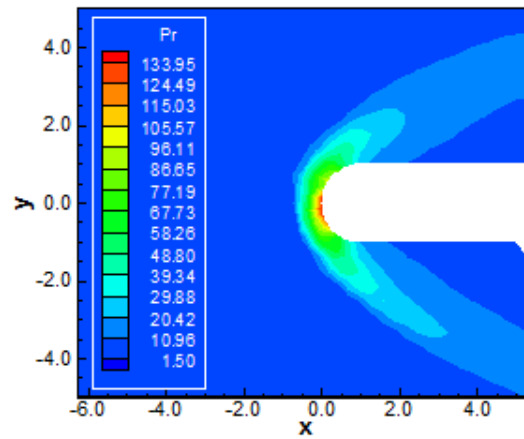


Figure 21: Pressure contours (LGL-LS)

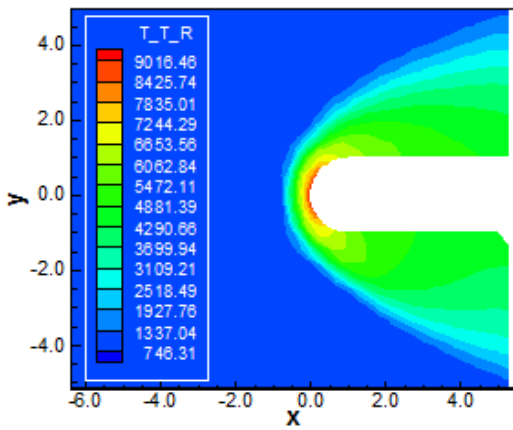


Figure 22: Translational/rotational temperature contours (LGL-VL)

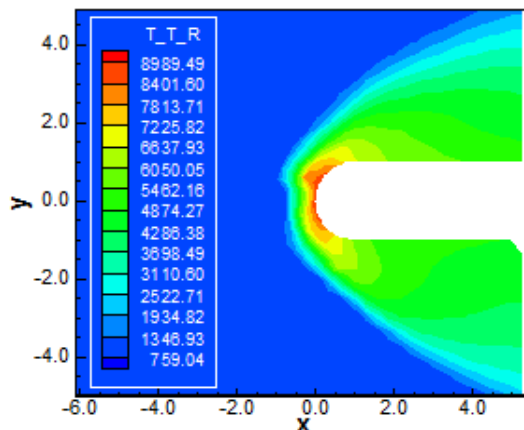


Figure 23: Translational/rotational temperature contours (LGL-LS)

Blunt Body Viscous Solutions

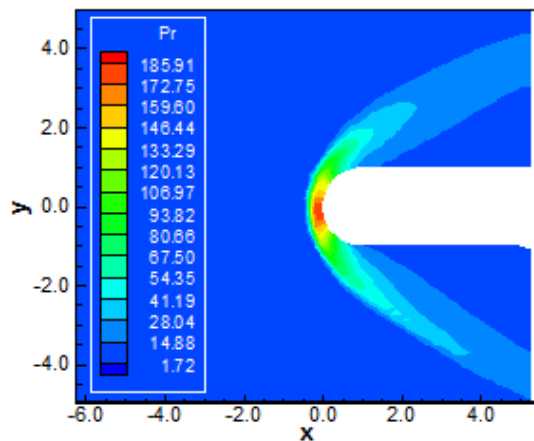


Figure 24: Pressure contours (CGR-LS)

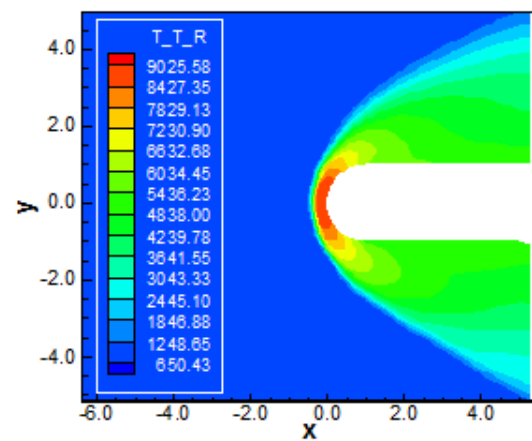


Figure 25: Translational/rotational temperature contours (CGR-LS)

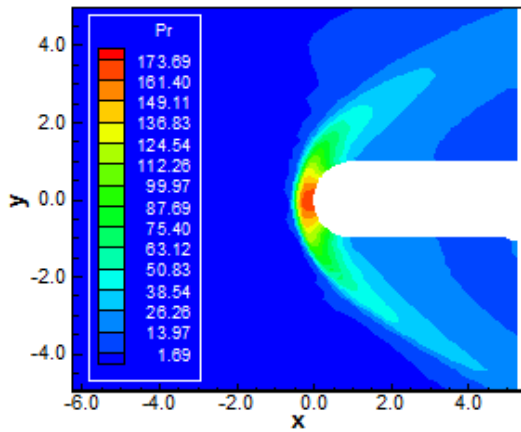


Figure 26: Pressure contours (CGL-VL)

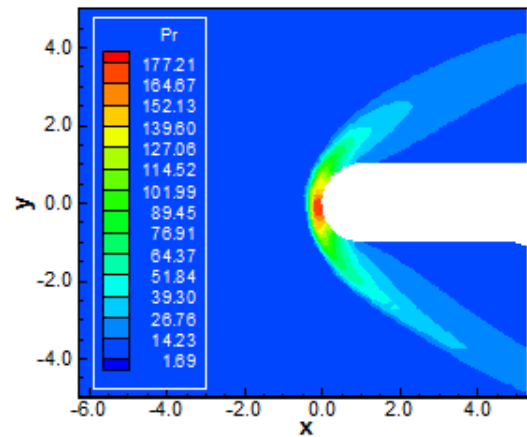


Figure 27: Pressure contours (CGL-LS)

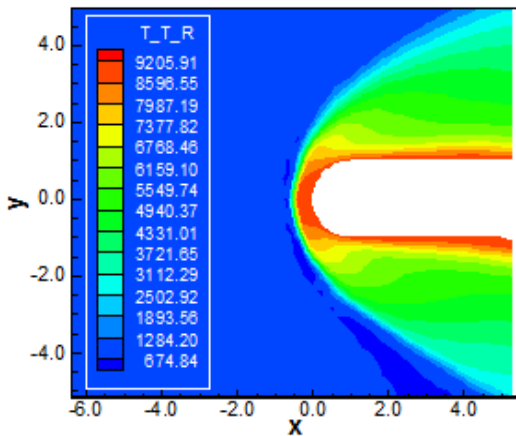


Figure 28: Translational/rotational temperature contours (CGL-VL)

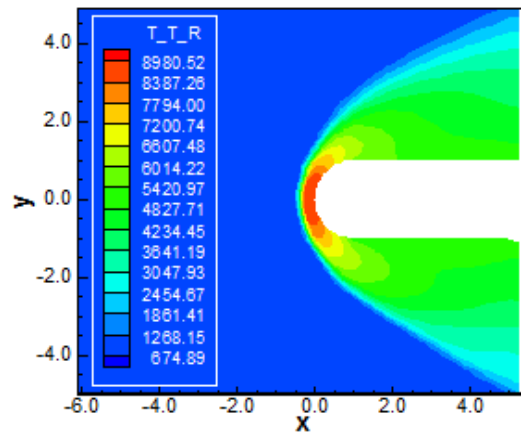


Figure 29: Translational/rotational temperature contours (CGL-LS)

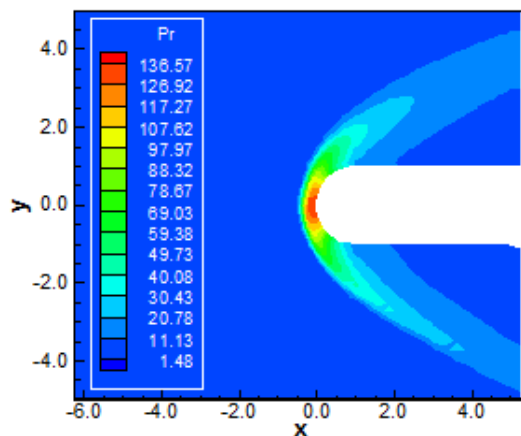


Figure 30: Pressure contours (LGR-VL)

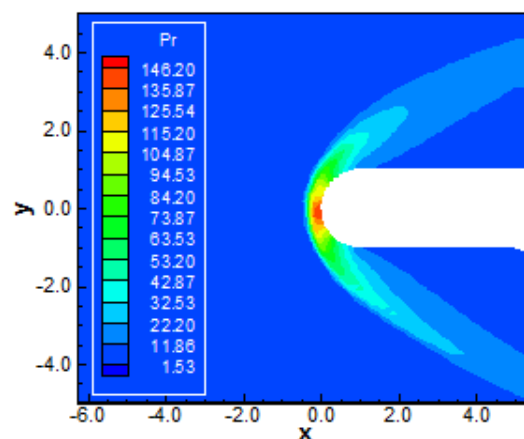


Figure 31: Pressure contours (LGR-LS)



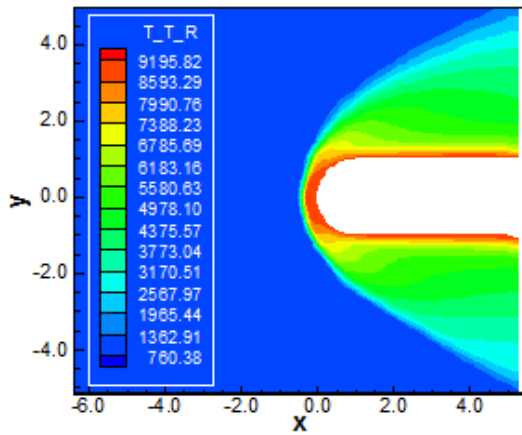


Figure 32: Translational/rotational temperature contours (LGR-VL)

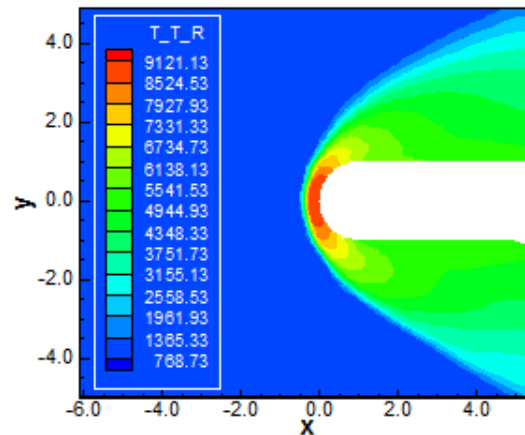


Figure 33: Translational/rotational temperature contours (LGR-LS)

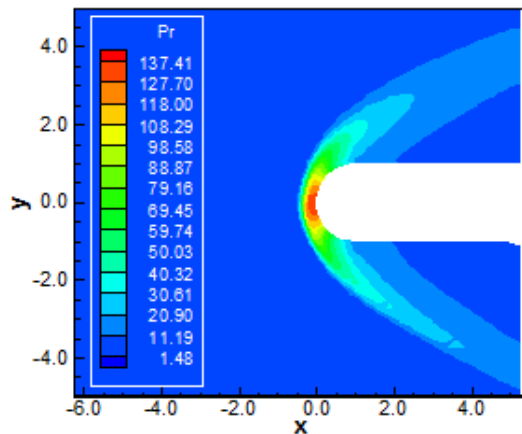


Figure 34: Pressure contours (LGL-VL)

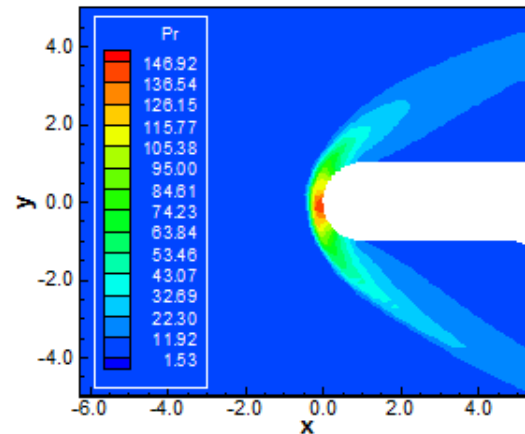


Figure 35: Pressure contours (LGL-LS)

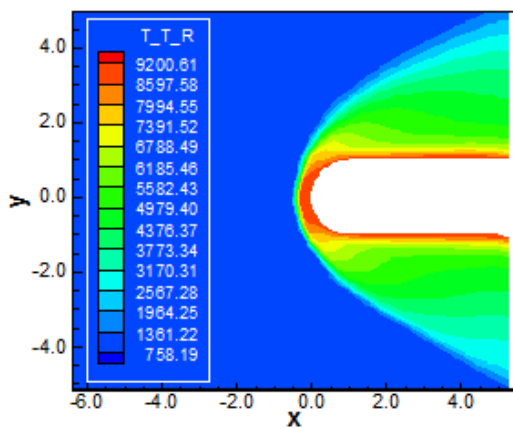


Figure 36: Translational/rotational temperature contours (LGL-VL)

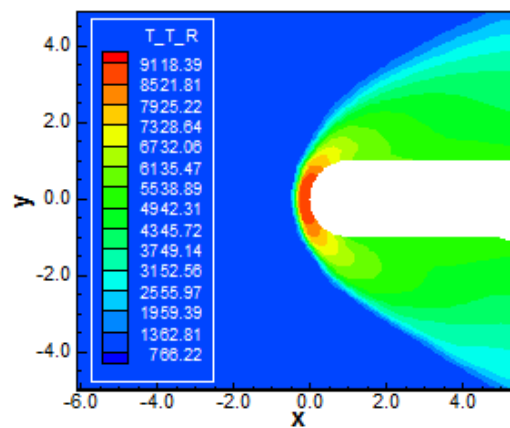


Figure 37: Translational/rotational temperature contours (LGL-LS)

Double Ellipse Inviscid Solutions

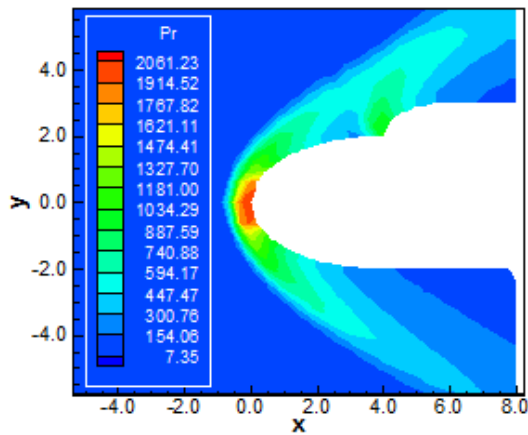


Figure 38: Pressure contours (CGR-VL)

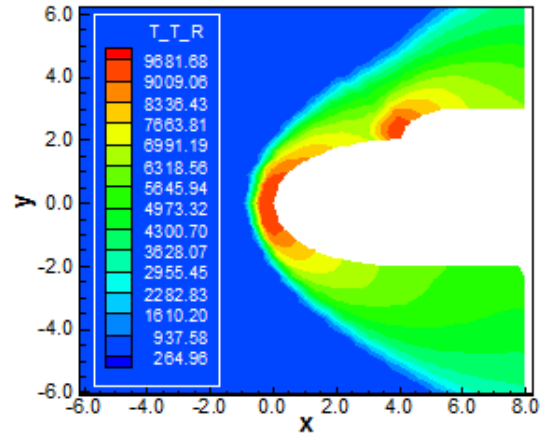


Figure 39: Translational/rotational temperature contours (CGR-VL)

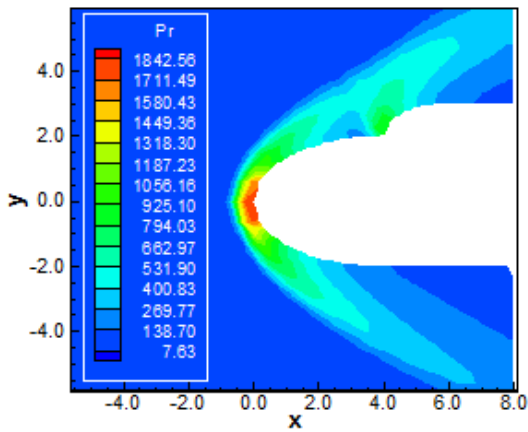


Figure 40: Pressure contours (CGL-VL)

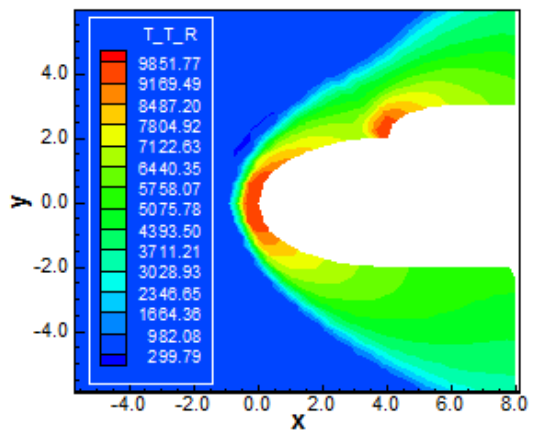


Figure 41: Translational/rotational temperature contours (CGL-VL)

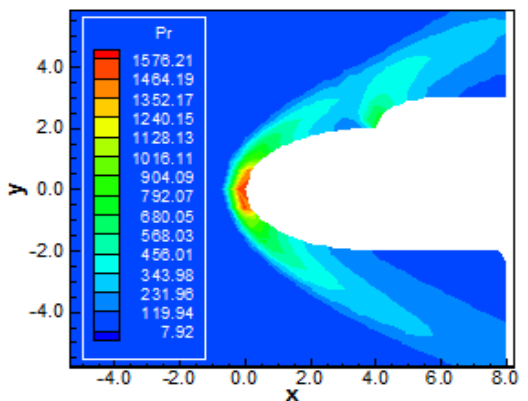


Figure 42: Pressure contours (LGR-VL)

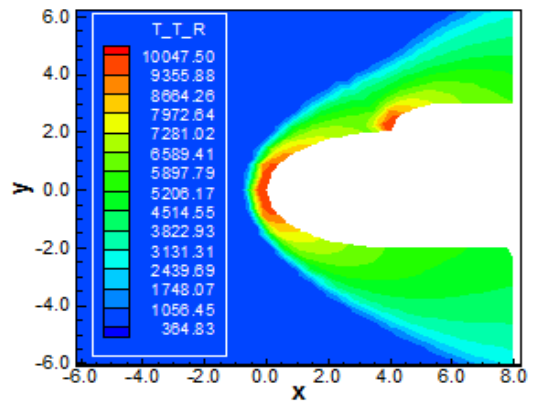


Figure 43: Translational/rotational temperature contours (LGR-VL)



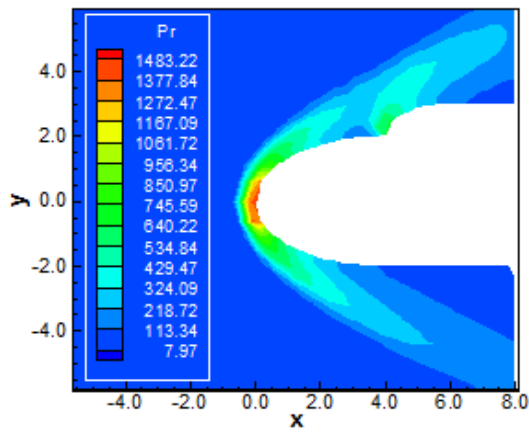


Figure 44: Pressure contours (LGL-VL)

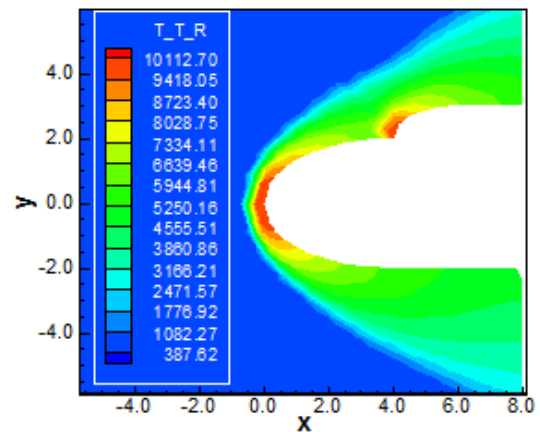


Figure 45: Translational/rotational temperature contours (LGL-LS)

Double Ellipse Viscous Solutions

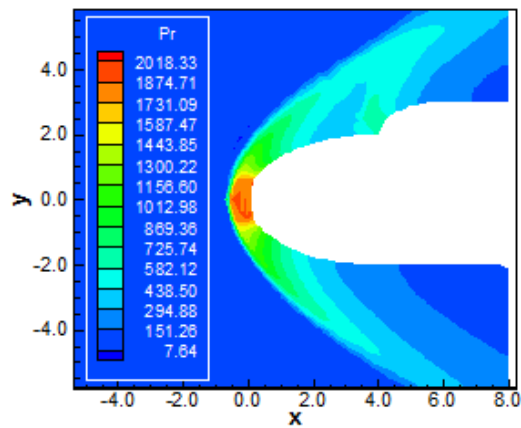


Figure 46: Pressure contours (CGL-VL)

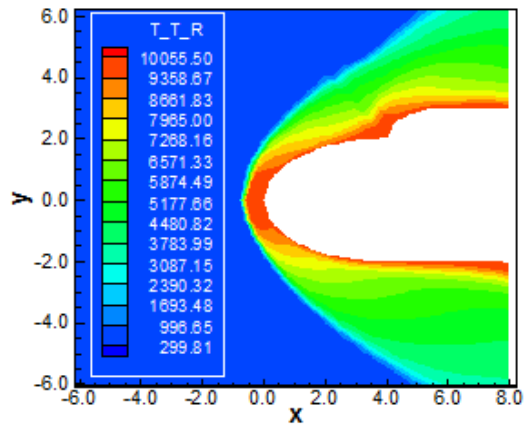


Figure 47: Translational/rotational temperature contours (CGL-VL)

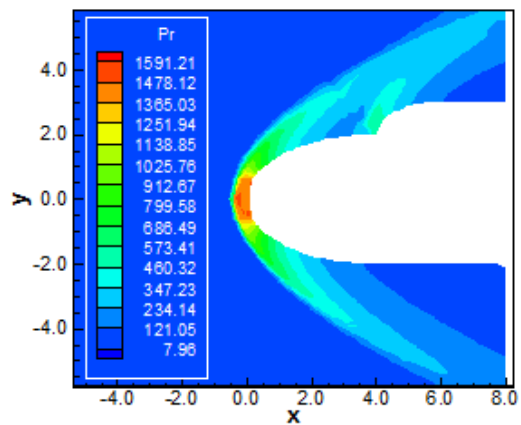


Figure 48: Pressure contours (LGR-VL)

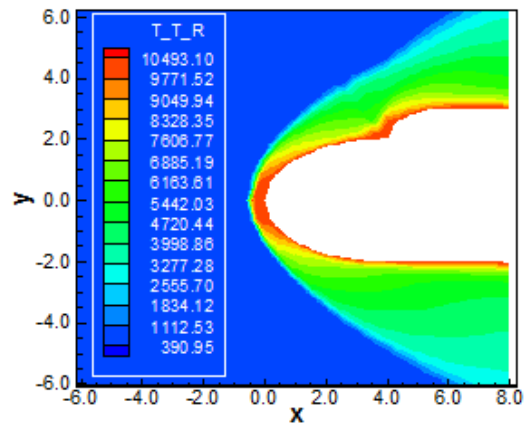


Figure 49: Translational/rotational temperature contours (LGR-VL)

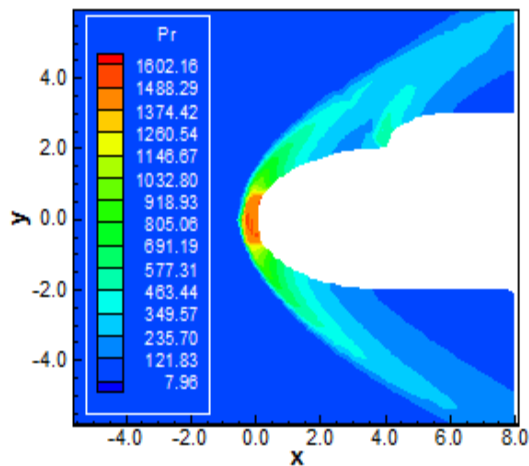


Figure 50: Pressure contours (LGL-VL)

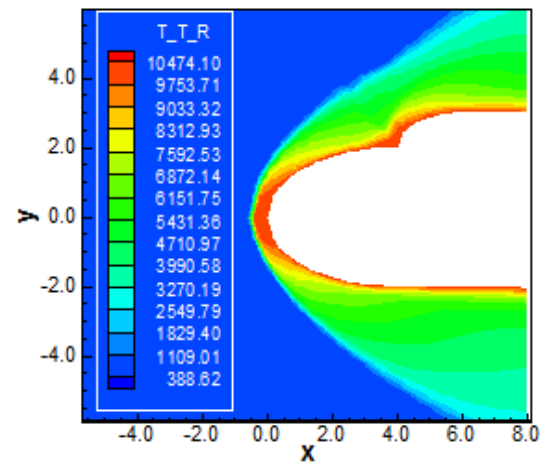


Figure 51: Translational/rotational temperature contours (LGL-VL)

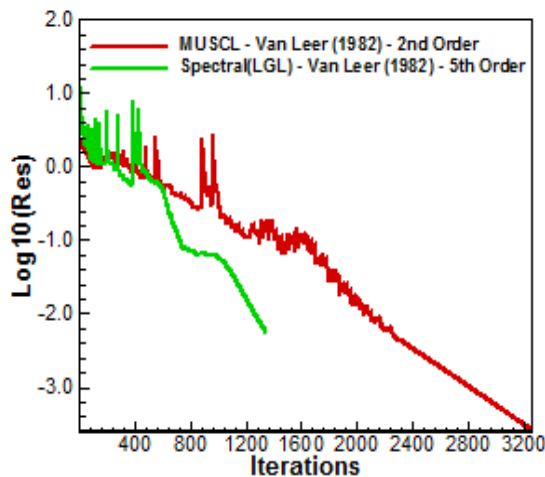


Figure 52: Convergence histories comparison (VL)

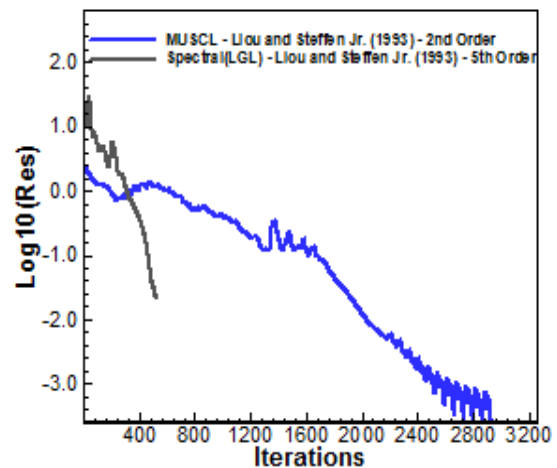


Figure 53: Convergence histories comparison (LS)

9. Conclusions

In the present work, a study involving a spectral method to solve the reactive Euler and Navier-Stokes equations was performed. The Euler and Navier-Stokes equations, in conservative and finite volume contexts, employing unstructured spatial discretization, on a condition of thermochemical non-equilibrium, were studied. The spectral method presented in this work employed collocation points and variants of Chebyshev and Legendre interpolation functions were analyzed. High-order studies were accomplished to verify the accuracy of the spectral method. The “hot gas” hypersonic flows around a blunt body, and around a double ellipse in two-dimensions were simulated. The [34-35] flux vector splitting algorithms were applied to execute the numerical experiments. The Euler backward integration method was employed to march the schemes in time. The convergence process was accelerated to steady state condition through a spatially variable time step procedure, which had proved effective gains in terms of computational acceleration (see [36-37]). The reactive simulations involved Earth atmosphere chemical model of five species and seventeen reactions, based on the [38] model. N, O, N₂, O₂, and NO species were used to accomplish the numerical comparisons. The results have indicated that the Chebyshev collocation point variants are more accurate in terms of stagnation pressure estimations, with errors inferior to 17.00% in the worst case, and in terms of lift coefficient estimations. Moreover, the Legendre collocation point variants are more computationally efficient.



As final conclusion, it is possible to highlight that, for the blunt body problem, the [34] scheme in the viscous case using Chebyshev-Gauss-Lobatto collocation points had the best performance in estimating the stagnation pressure, and the lift aerodynamic coefficient was best estimated by the [35] scheme as using the Chebyshev-Gauss-Lobatto collocation points; and for the double ellipse problem, the [34] scheme in the inviscid case using Chebyshev-Gauss-Radau collocation points had the best performance in estimating the stagnation pressure. Moreover, the best performance of the numerical schemes, for the 5th order of accuracy, was due to the [35] one, when using the Legendre-Gauss-Lobatto collocation points, employing a CFL of 0.20, and converging in 523 iterations, in the blunt body problem, whereas for the 8th order of accuracy, the best performance of the numerical schemes was due to the [35] one, when using the Legendre-Gauss-Radau collocation points, employing a CFL of 0.20, and converging in 1,074 iterations, also in the blunt body problem.

Finally, to close this work, the computational cost of the numerical schemes using the several types of collocation points was presented in Tab. 10. For the inviscid case, the cheapest combination was the [34] scheme using Chebyshev-Gauss-Radau collocation points with a cost of 0.0001115 sec/per-volume/per-iteration, whereas for the viscous case the cheapest was due to the [35] scheme coupled with the Chebyshev-Gauss-Radau collocation points with a cost of 0.0002139 sec/per-volume/per-iteration.

10. Motivation and Novelty

The motivation to study spectral methods applied to reentry flow was enormous because of some papers in the CFD literature report for such methods as the state of art of high order resolution. The intention of this paper was to propose a different spectral method that was of easy implementation and conformed about author's ideas of treating the governing equations of fluid flow. The formulation presented here is for a thermochemical non-equilibrium condition and a two-temperature model. The comparisons involving the residual histories of MUSCL and of spectral method were very important to confirm that our numerical implementation was correct and also the potentiality of the method. Two physical problems were also a challenge that we accepted to lead with. The results with good accuracy represent a motivation to extend the present formulation to more species and different chemical conditions.

The novelty of the present study was to implement this different spectral method to treat thermochemical non-equilibrium reentry flows and to formulate the appropriate equations for accepting this method. The robustness and convergence features of this spectral method are very impressive. While the first author had to use CFL numbers of order 0.10 for his MUSCL explicit method, CFL numbers as great as 0.40 for his explicit spectral method were of common use. The proposed spectral method is different from the standard spectral ones on a sense that in the latter, the differential equations and the solution method are discretized with spectral tools, whereas in the former, only the vector of conserved variables and the convective fluxes should be discretized according to the spectral tools. The result is a robust and fast solver to treat the fluid-dynamic of reentry flows.

11. Future Works

For the future, the author should extend the present formulation for a seven species chemical model under the condition of thermochemical non-equilibrium in two-dimensions. After that, he should extend to eleven species in two-dimensions until to arrive to the desired three-dimensional studies. Finally, its implementation with turbulence effects and magnetic field actuation, that the first author consider as the state of the art project, is an objective to be reached, in both, two- and three-dimensions.

References

- [1]. Barnes CJ, Huang GP, Shang JS. A high resolution spectral method for the compressible Navier-Stokes equations. AIAA Paper 2011-0049; 2011.
- [2]. Huang P, Wang ZJ, Liu Y. An implicit space-time spectral difference method for discontinuity capturing using adaptive polynomials. AIAA Paper 2005-5255; 2005.
- [3]. Huang P. High order discontinuity capturing using adaptive polynomials. AIAA Paper 2006-0305; 2006.



- [4]. Steger JL, Warming RF. Flux vector splitting of the inviscid gas dynamic equations with application to finite difference methods. *Journal of Computational Physics*. 1981; 40: 263-293.
- [5]. Hughes T. *The finite element method, linear static and dynamic finite element analysis*, Prentice-Hall, Inc.
- [6]. Lele S. Compact finite difference schemes with spectral-like resolution. *Journal of Computational Physics*. 1991; 103: 16-42.
- [7]. Gottlieb D, Orszag S. *Numerical analysis of spectral methods: theory and applications*. Society for industrial and applied mathematics, Philadelphia.
- [8]. Hussaini MY, Kopriva DA, Salas MD, Zang TA. Spectral methods for the Euler equations: Part I – Fourier methods and shock capturing. *AIAA Journal*. 1985; 23(1): 64-70.
- [9]. Slater JC. Electronic energy bands in metal. *Physical Review*. 1934; 45: 794-801.
- [10]. Barta J. Über die näherungsweise Lösung einigerzweidimensionalerelastizitätsaufgaben. *Zeitschrift fuer Angewandte Mathematik und Mechanik*. 1937; 17: 184-185.
- [11]. Frazer RA, Jones WP, Skan SW. *Approximation to functions and to the solutions of differential equations*. Aeronautical Research Council, London. R&M 1799; 1937.
- [12]. Lanczos CL. Trigonometric interpolation of empirical and analytic functions. *Journal of Mathematics and Physics*. 1938; 17: 123-199.
- [13]. Gottlieb D, Lustman L, Orszag SA. Spectral calculations of one-dimensional inviscid compressible flows. *SIAM Journal of Scientific and Statistical Computation*. 1981; 2: 296-310.
- [14]. Taylor TD, Meyers RB, Albert JH. Pseudospectral calculations of shock waves, rarefaction waves and contact surfaces. *Computers and Fluids*. 1981; 9: 469-473.
- [15]. Zang TA, Hussaini MY. Mixed spectral-finite difference approximations for slightly viscous flows. *Proceedings of the 7th International Conference on Numerical Methods in Fluid Dynamics*. Edited by W. C. Reynolds and R. W. Mac Cormack. *Lecture Notes in Physics*. 1981; 141: 461-466.
- [16]. Narayan JR, Girimaji SS. Turbulent reacting flow computations including turbulence-chemistry interactions. *AIAA Paper 92-0342*; 1992.
- [17]. Gnoffo PA, Gupta RN, Shinn JL. Conservation equations and physical models for hypersonic flows in thermal and chemical nonequilibrium. *NASA TP 2867*; 1989.
- [18]. Liu M, Vinokur M. Upwind algorithms for general thermo-chemical nonequilibrium flows. *AIAA Paper 89-0201*; 1989.
- [19]. Park C. Radiation enhancement by nonequilibrium in Earth's atmosphere. *Journal of Spacecraft and Rockets*. 1985; 22(1): 27-36.
- [20]. Park C. Problem of rate chemistry in the flight regimes of aeroassisted orbital transfer vehicles. *Thermal design of aero-assisted orbital transfer vehicles*. *Progress in Astronautics and Aeronautics*. Edited by H. F. Nelson, AIAA, NY. 1985; 96: 511-537.
- [21]. Gnoffo PA. Three-dimensional AOTV flowfields in chemical nonequilibrium. *AIAA Paper 86-0230*; 1986.
- [22]. Li CP. Implicit methods for computing chemically reacting flow. *NASA TM-58274*; 1986.
- [23]. Lee JH. Basic governing equations for the flight regimes of aeroassisted orbital transfer vehicles. *Thermal design of aeroassisted transfer vehicles*. *Progress in Astronautics and Aeronautics*, AIAA. 1985; 96: 3-53.
- [24]. Park C. Convergence of computation of chemically reacting flows. *Thermophysical aspects of reentry flows*. *Progress in Astronautics and Aeronautics*. Edited by J. N. Moss and C. D. Scott, AIAA, NY. 1986; 103: 478-513.
- [25]. Park C. Assessment of two-temperature kinetic model for dissociating and weakly-ionizing nitrogen. *AIAA Paper 86-1347*; 1986.
- [26]. Park C. Calculation of nonequilibrium radiation in the flight regimes of aeroassisted orbital transfer vehicles. *Thermal design of aeroassisted orbital transfer vehicles*. *Progress in Astronautics and Aeronautics*. Edited by H. F. Nelson, AIAA, NY. 1985; 96: 395-418.
- [27]. Park C. Nonequilibrium air radiation (NEQAIR) program: User's manual. *NASA TM-86707*; 1985.



- [28]. Turkel E, Van Leer B. Flux-vector splitting and Runge-Kutta methods for the Euler equations. ICASE Report 84-27; also NASA CR 172415; 1984.
- [29]. Riggins DW, Walters RW, Pelletier D. The use of direct solvers for compressible flow computations. AIAA Paper 88-0229; 1988.
- [30]. Mavriplis D, Jameson A. Multigrid solution of the Euler equations on unstructured and adaptive meshes. ICASE Report 87-53; also NASA CR 178346; 1987.
- [31]. Barth TJ, Jespersen DC. The design and application of upwind schemes on unstructured meshes. AIAA Paper 89-0336; 1989.
- [32]. Stoufflet B, Périaux J, Fezoui F, Dervieux A. Numerical simulation of 3-D hypersonic Euler flows around space vehicles using adapted finite-elements. AIAA Paper 87-0560; 1987.
- [33]. Whitaker DL. Two-dimensional Euler computations on a triangular mesh using an upwind, finite-volume scheme. Ph.D. Thesis. Dept. of Aerospace and Ocean Engineering, Virginia Polytechnic Inst. and State Univ., Blacksburg, VA; 1988.
- [34]. Van Leer B. Flux-vector splitting for the Euler equations. Lecture Notes in Physics, Springer Verlag, Berlin. 1982; 170: 507-512.
- [35]. Liou M, Steffen Jr. CJ. A new flux splitting scheme. Journal of Computational Physics, 1993; 107: 23-39.
- [36]. Maciel ESG. Simulations in 2D and 3D applying unstructured algorithms, Euler and Navier-Stokes equations – Perfect gas formulation. Saarbrücken, Deutschland: Lambert Academic Publishing (LAP). 2015; Ch. 1: 26-47.
- [37]. Maciel ESG. Simulations in 2D and 3D applying unstructured algorithms, Euler and Navier-Stokes equations – Perfect gas formulation. Saarbrücken, Deutschland: Lambert Academic Publishing (LAP). 2015; Ch. 6: 160-181.
- [38]. Saxena SK, Nair MT. An improved Roe scheme for real gas flow. AIAA Paper 2005-0587; 2005.
- [39]. Hussaini MY, Streett CL, Zang TA. Spectral methods for partial differential equations. ICASE Report No. 83-46; 1983.
- [40]. Davis PA, Rabinowitz P. Numerical integration. Blaisdell Publishing Co.; 1967.
- [41]. Canuto C, Hussaini MY, Quarteroni A, Zang TA. Spectral methods evolution to complex geometries and applications to fluid dynamics. Scientific Computation Springer; 2007.
- [42]. Prabhu RK. An implementation of a chemical and thermal nonequilibrium flow solver on unstructured meshes and application to blunt bodies. NASA CR-194967; 1994.
- [43]. Maciel ESG. Hypersonic reactive flow simulations in two-dimensions, chemical and thermochemical non-equilibrium conditions. Saarbrücken. Deutschland: Lambert Academic Publishing (LAP). 2015; Ch. 3: 174-247.
- [44]. Maciel ESG. Hypersonic reactive flow simulations in two-dimensions, chemical and thermochemical non-equilibrium conditions. Saarbrücken. Deutschland: Lambert Academic Publishing (LAP). 2015; Ch. 4: 248-332.
- [45]. Ait-Ali-Yahia D, Habashi WG. Finite element adaptive method for hypersonic thermochemical nonequilibrium flows. AIAA Journal. 1997; 35(8): 1294-1302.
- [46]. Radespiel R, Kroll N. Accurate flux vector splitting for shocks and shear layers. Journal of Computational Physics. 1995; 121: 66-78.
- [47]. Long LN, Khan MMS, Sharp HT. Massively parallel three-dimensional Euler / Navier-Stokes method. AIAA Journal. 1991; 29(5): 657-666.
- [48]. Vincent WG, Kruger Jr. CH. Introduction to physical gas dynamics. Malabar, Florida, EUA: Krieger Publishing Company. 2002; Ch. 1: 1-26.
- [49]. Fox RW, McDonald AT. Introdução à mecânica dos fluidos. Guanabara Editor; 1988.
- [50]. Maciel ESG. Simulação numérica de escoamentos supersônicos e hipersônicos utilizando técnicas de dinâmica dos fluidos computacional. Doctoral Thesis. ITA, CTA, São José dos Campos, SP, Brazil; 2002.



- [51]. Maciel ESG. Comparison among MUSCL, ENO and WENO procedures as applied to reentry flows in 2D. *Computational and Applied Mathematics Journal*. 2015; 1(5): 355-377.
- [52]. Anderson Jr. JD. *Fundamentals of aerodynamics*. McGraw-Hill, Inc., 5th Edition, 1008p.; 2010.

